The OLYMPUS Experiment

N. Akopov, A. Avetisyan, G. Elbakian, G. Karyan, H. Marukyan, A. Movsisyan[1], H. Vardanyan, V. Yeganov

Alikhanyan National Science Laboratory (Yerevan Physics Institute), Yerevan, Armenia

R. Alarcon, L.D. Ice

Arizona State University, Tempe, AZ, USA

D. Bayadilov, R. Beck, D. Eversheim, Ch. Funke, Ph. Hoffmeister, P. Klassen, A. Thiel

Rheinische Friedrich Wilhelms Universität Bonn, Bonn, Germany

F. Brinker, N. D'Ascenzo, N. Görrissen, J. Hauschildt, Y. Holler, D. Lenz, U. Schneekloth

Deutsches Elektronen-Synchrotron, Hamburg, Germany

R. Kaiser, I. Lehmann[2], S. Lumsden, M. Murray, G. Rosner[2], B. Seitz

University of Glasgow, Glasgow, United Kingdom

O. Ates, J. Diefenbach[3], M. Kohl

Hampton University, Hampton, VA, USA

R. De Leo, R. Perrino

Istituto Nazionale di Fisica Nucleare, Bari, Italy

V. Carassiti, G. Ciullo, M. Contalbrigo, P. Lenisa, M. Statera

Università di Ferrara and Istituto Nazionale di Fisica Nucleare, Ferrara, Italy

---

[*]Corresponding Author

Email address: `hasell@mit.edu` (D.K. Hasell)

[1]Also with Università di Ferrara and Istituto Nazionale di Fisica Nucleare, Ferrara, Italy

[2]Also with the Facility for Antiproton and Ion Research, Darmstadt, Germany

[3]Currently with Johannes Gutenberg-Universität, Mainz, Germany

[4]Currently with RIKEN, Nishina Center, Advanced Meson Science Laboratory, Japan

[5]Currently with Varian Medical Systems, Bonn, Germany

[6]Currently with Brookhaven National Laboratory, Brookhaven, NY, USA

Preprint submitted to Nuclear Instruments and Methods A *October 19, 2013*

E. Cisbani, S. Frullani

Istituto Nazionale di Fisica Nucleare, Rome, Italy

B. Gläser, D. Khaneft, Y. Ma[4], F. Maas, R. Perez Benito, D. Rodríguez Piñeiro

Johannes Gutenberg-Universität, Mainz, Germany

J.C. Bernauer, J. Bessuille, B. Buck, T.W. Donnelly, K. Dow, D.K. Hasell[*], B. Henderson, J. Kelsey, R. Milner, C. O'Connor, R.P. Redwine, R. Russell, A. Schmidt, C. Vidal, A. Winnebeck[5]

Massachusetts Institute of Technology, Cambridge, MA, USA

V.A. Andreev, S. Belostoski, G. Gavrilov, A. Izotov, A. Kiselev[6], A. Krivshich, O. Miklukho, Y. Naryshkin, D. Veretennikov

Petersburg Nuclear Physics Institute, Gatchina, Russia

J.R. Calarco

University of New Hampshire, Durham, NH, USA

Abstract

OLYMPUS was designed to measure the cross section ratio of positron-proton to electron-proton elastic scattering, with the goal of determining the contribution of two-photon exchange to elastic scattering. Two-photon exchange might resolve the discrepancy between measurements of the proton's form factor ratio $\mu_p G_E^p/G_M^p$ made using polarization techniques and those made in unpolarized experiments. To make this determination, OLYMPUS operated on the DORIS storage ring at DESY, alternating beteen electron and positron beams at 2.01 GeV incident on an internal hydrogen gas target. The experiment used a toroidal magnetic spectrometer instrumented with drift chambers and time of flight detectors to measure rates for elastic scattering over the polar angular range of approximately 25°–75°. A symmetric Møller / Bhabha calorimeter at 1.292° and telescopes of GEM and MWPC detectors at 12° served as luminosity monitors. A total luminosity of approximately 4.5 fb^{-1} was collected over two running periods in 2012. This paper provides details on the accelerator, target, detectors, and operation of the experiment.

Keywords: elastic electron scattering, elastic positron scattering, two-photon exchange, form-factor ratio
2010 MSC: 25.30.Bf, 25.30.Hm, 13.60.Fz, 13.40.Gp, 29.30.-h

---

1. Introduction

Electron scattering has long been an important tool for studying the structure of nucleons. The strength of the technique lies in the predominantly electromagnetic nature of the interaction. The electron is, to the best of our knowledge, a point-particle, and its vertex is well described by quantum electrodynamics. The interaction is mediated by a photon, whose momentum transfer sets a size scale for the structures that are probed in the scattering reaction. A low-momentum photon can only "see" the size of the nucleon, but by increasing the momentum transfer, the photon is sensitive to the nucleon's internal distribution of charge and magnetism, parameterized by form factors G_E and G_M. At even higher momentum transfers, deep inelastic scattering reveals the distributions of the quarks and gluons, which are ultimately responsible for the observed form factors. The synthesis of data at all different momentum scales can verify and guide our theoretical understanding of the nucleon.

Polarized beams and targets offer another window into the structure of nucleons. Recently, measurements of the electric to magnetic form factor ratio of the proton, $\mu_p G_E^p / G_M^p$, using polarization techniques (1–8) have shown a dramatic discrepancy in comparison with the ratio obtained using the traditional Rosenbluth technique in unpolarized cross section measurements (9–12) as shown in Fig. 1. This discrepancy might arise from a significant contribution to the elastic electron-proton cross section from hard two-photon exchange (13–18), a process which is neglected in the standard radiative corrections procedures. Since there is not a theoretical consensus on the size of this contribution (13–24), definitive measurements are needed to determine if two-photon exchange resolves the form factor discrepancy.

To address this question, the OLYMPUS Experiment was proposed to measure the ratio between the positron-proton and electron-proton elastic scattering cross sections. In the single-photon exchange approximation, this ratio is unity, while the next-to-leading interference of one-photon and two-photon exchange diagrams changes sign between electron and positron scattering. Measurements from the 1960s indicated some deviation in the ratio from unity, but the uncertainties were large, as can be seen in Fig. 2.

The OLYMPUS experiment was approved for three months of dedicated operation at the DORIS electron/positron storage ring at DESY, in Hamburg, Germany. Alternating electron and positron beams were directed on a fixed proton target, with the scattered leptons and recoiling protons detected

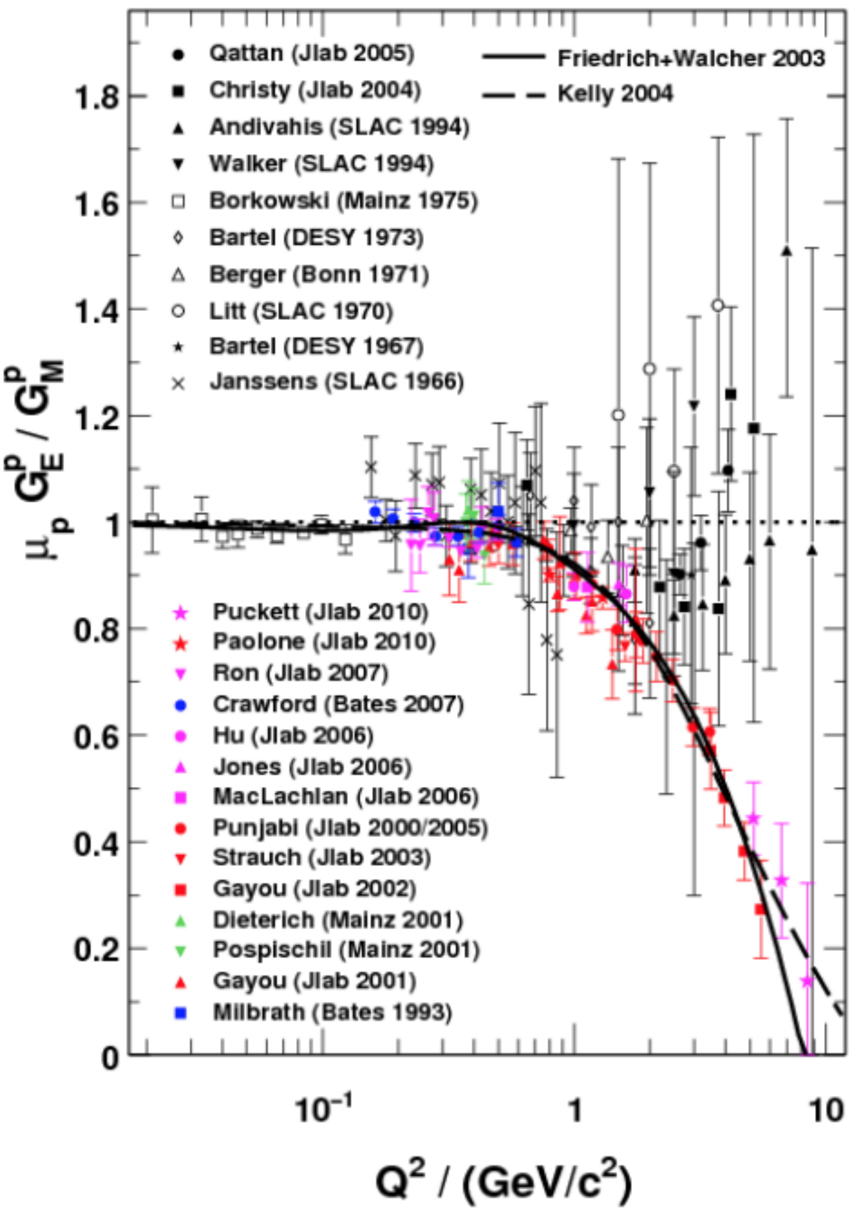

Fig. 1: Ratio of proton form factors $\mu_p G_E^p/G_M^p$ as a function of Q^2 showing results from unpolarized measurements in black and recent data measured using polarized techniques.

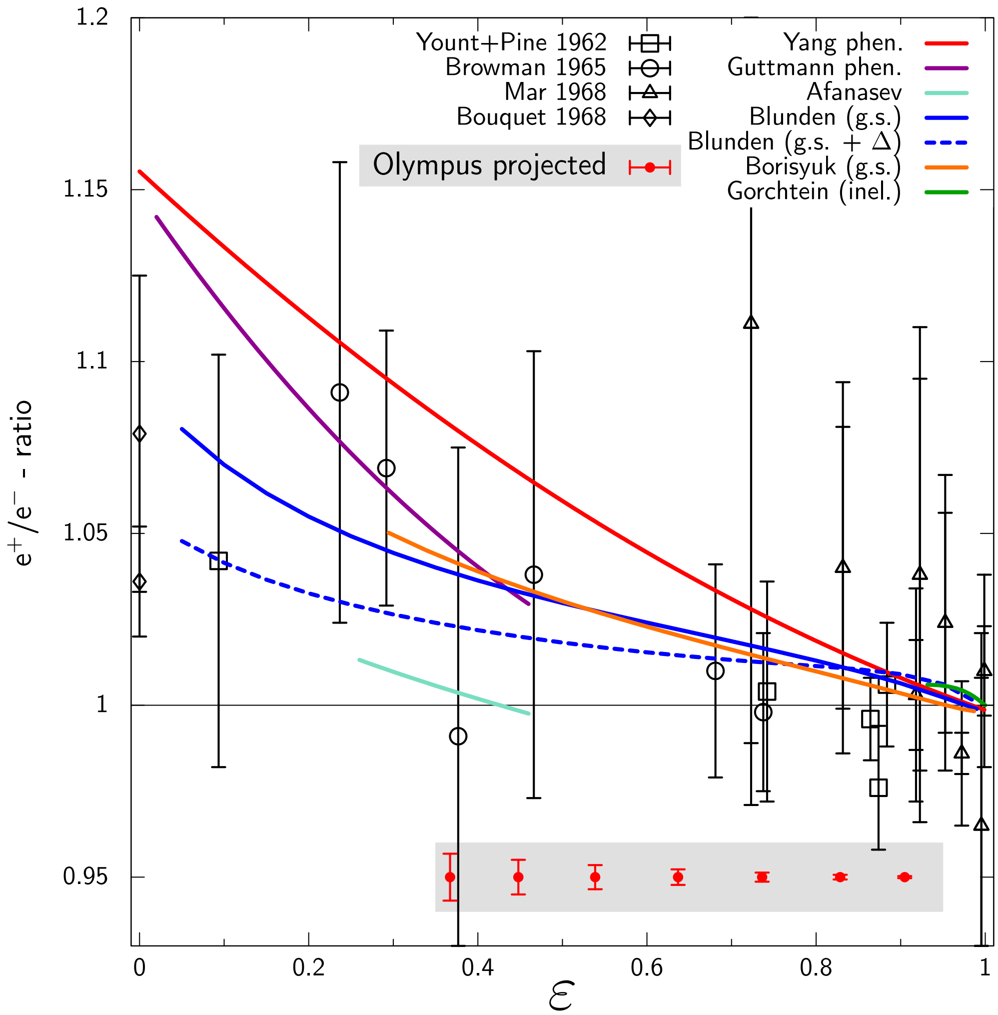

Fig. 2: Ratio of positron to electron elastic scattering cross section as a function of ϵ showing existing data, some theoretical predictions, and projected OLYMPUS data range and uncertainties. Theory calculations are from (16–18, 21–24).

in coincidence over a wide range of scattering angles. An unpolarized hydrogen gas target was designed and built at MIT and installed internally to the DORIS ring. The former BLAST detector was shipped from MIT-Bates to DESY and placed around the target. The detector used a toroidal magnetic field with a left/right symmetric arrangement of tracking detectors and time of flight scintillators. In addition, three new detector systems were designed and built to monitor the luminosity during the experiment; triple GEM detectors from Hampton and MWPC detectors from Gatchina were mounted in telescopes at 12°, while symmetric Møller/Bhabha calorimeters from Mainz were positioned at 1.292°. The Bonn group provided the software and hardware for the data acquisition system. The trigger and slow control systems were developed by MIT.

The OLYMPUS Experiment collected data in two periods: the February period (January 20 - February 27, 2012) and the Fall period (October 24, 2012 - January 2, 2013). During the February period, the beam species was typically changed daily, and the magnet polarity was changed randomly, but equally, every 6 hours. For the February data run, there was a leak in the target gas supply such that only a fraction of the measured flow reached the target cell. Because of this, a lower than expected luminosity was obtained. The gas leak was repaired in the summer so that it was possible to achieve high luminosity in the Fall period. However, it was discovered that at high luminosity and negative magnet polarity too many electrons were bent into the wire chambers, preventing their operation. After several tests and attempts to remedy this, it was decided to operate at high luminosity but primarily with positive magnet polarity for most of the Fall period.

The following sections describe the accelerator, target, detectors, data acquisition, and operation in more detail.

2. DORIS Storage Ring at DESY

The DORIS storage ring at DESY originally began operation in 1974 as an electron-electron and electron-positron collider. After its long and successful operation for particle physics research, DORIS was dedicated to synchrotron radiation studies in 1993. Since DORIS had access to both a positron and electron source and could circulate both species at several GeV energies, it was a natural candidate for the OLYMPUS experiment. Additionally, the infrastructure at the location in the beamline of the former Argus Experiment (25) provided an excellent match to the size and needs of OLYMPUS. In 2009, the shutdown of DORIS was scheduled for the end of 2012, placing a tight time constraint on OLYMPUS.

Although the DORIS accelerator and the ARGUS detector site were well suited to the OLYMPUS Experiment, several modifications were required. In particular, a number of considerations were necessary to allow DORIS to continue to operate as a synchrotron light source after OLYMPUS was installed (although not during OLYMPUS data taking). These included:

- RF cavities that had been installed at the detector site had to be relocated 26 m upstream.

- An additional quadrupole was installed on each side (± 7 m) of the OLYMPUS interaction region to reduce the beam size for the OLYMPUS target while not significantly affecting the beam profile in synchrotron radiation source elements. This was necessary due to the impracticality of removing the OLYMPUS target for synchrotron runs.

- The OLYMPUS target required cooling during synchrotron radiation runs due to the wakefield heating caused by the 150 mA, 4.5 GeV, 5-bunch beam.

- A number of tests and improvements were required to achieve the 10-bunch, 2.01 GeV beam conditions for OLYMPUS operation with adequate currents and lifetimes, including the implementation of a multi-bunch feedback system.

A key feature of the OLYMPUS experiment was the frequent switching between e^- and e^+ beams. The DORIS pre-accelerators were already able to switch between electrons and positrons within approximately 10 minutes, but the extraction from the pre-accelerators to DORIS, the transport line, and the DORIS ring needed several modifications:

- The high voltage pulse power supplies for the pre-accelerator extraction and the DORIS injection kickers had to be rebuilt.

- The septa magnets for pre-accelerator extraction and DORIS injection were modified to serve as bipolar devices.

- Remotely-controlled polarity switches for a number of 800 A magnet power supplies had to be constructed and installed.

The daily switching of the beam species for OLYMPUS posed a challenge for the parallel operation of DORIS and the PETRA storage ring, which shared the same pre-accelerators. While PETRA did not operate during the February run, the procedure for switching the polarity of the pre-accelerators was optimized to accommodate parallel operation during the Fall run. With these improvements, PETRA could be refilled in approximately five minutes, causing only a small delay for DORIS refills.

Since the injection into DORIS occurred at full energy, it was possible to run in top-up mode to achieve higher average current, and hence more luminosity. The injection process was optimized to minimize beam losses, which prevented excessive rates in the OLYMPUS detector (which would cause high voltage trips).

The radiation levels in the region downstream of the experiment increased when gas was added to the target, and additional shielding was installed to account for this. Also, the beam scrapers upstream of the experiment were optimized to minimize the noise rates in the experiment.

To monitor the beam energy, a dipole reference magnet was installed in series with the DORIS dipole magnets. This magnet included a rotating coil to measure the integrated field strength. The accelerator archive system monitored all relevant data, power supply currents for all magnets, beam position data, scraper positions, etc. and provided much of this information to the OLYMPUS slow control system.

3. Target and Vacuum Systems

The OLYMPUS experiment used an unpolarized, internal hydrogen gas target cooled to below 70 K. The hydrogen gas flowed into an open-ended, 600 mm long, elliptical target cell (Sec. 3.1). The target cell was housed in a scattering chamber (Sec. 3.2) that had thin windows to match the angular acceptance of the detectors. A tungsten collimator (Sec. 3.4) was also housed in the scattering chamber to prevent synchrotron radiation, beam halo, and off-momentum particles from striking the target cell. Additionally, a series of wakefield suppressors (Sec. 3.3) were necessary to reduce the heat load on the target cell. Finally, an extensive vacuum system (Sec. 3.5) of turbomolecular and Non-Evaporable Getter (NEG) pumps was employed to preserve the vacuum in the DORIS storage ring.

3.1. Target Cell

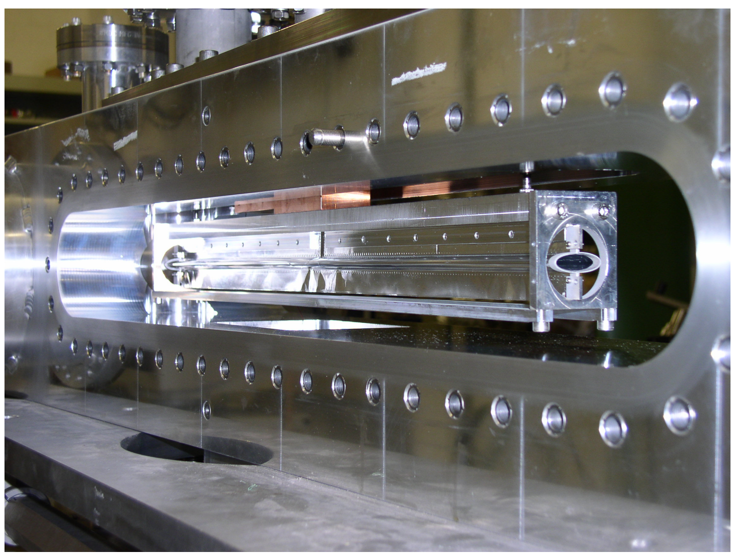

Fig. 3: Photograph of one of the OLYMPUS target cells mounted inside the scattering chamber.

The target cell consisted of an open-ended, elliptical cylinder (27 mm horizontal $\times$ 9 mm vertical $\times$ 600 mm long) made from 0.075 mm thick aluminum. The elliptical shape was chosen to match the DORIS beam envelope and was set to approximately the 10σ nominal horizontal and vertical beam width at the OLYMPUS interaction point to minimize the amount of beam halo striking the cell walls.

Several cells were fabricated over the course of the experiment at INFN, Ferrara. Cells were formed from two identical stamped sheets of aluminum that were spot welded together along the top and bottom seams. Each cell was mounted in a frame by a clamp that ran the entire length of the top seam. The frame was made of 6063 aluminum to provide high thermal conductivity at cryogenic temperatures. When installed in the scattering chamber, the cell and frame assembly was suspended from a flange in the top of the scattering chamber (shown in Fig. 3) and its position and orientation could be adjusted. The entire cell and frame assembly were cooled by a cryogenic coldhead. The assembly was wrapped in several layers of aluminized mylar to insulate it from thermal radiation. Without beam or gas flow, the target could reach temperatures below 40 K. During high luminosity running, a temperature of about 70 K was sustained.

During operation, hydrogen gas was flowed through the target cell. The hydrogen gas was produced by a commercial hydrogen generator and was controlled by a series of valves, buffer volumes, and mass flow controllers. The gas entered the cell at the center, from a tube that fit snuggly into an opening of the cell's top seam. The gas diffused outwards to the open ends of the cell, where it was removed by the vacuum system. This diffusion was slowed because the hydrogen quickly cooled to the temperature of the cell. The density distribution in the cell was triangular, with peak density at the center of the cell falling to zero density at either end. A flow rate of 1.5×10^{17} H_2 atoms per second was required to produce a target thickness of 3×10^{15} atoms cm^{-2}.

3.2. Scattering Chamber

The OLYMPUS scattering chamber (shown in Fig. 4) was 1.2 m long and was machined from a solid block of aluminum, with large area windows on the left and right faces. The windows were made of 0.25 mm thick 1100 aluminum, and nominally subtended a polar angular range of 8° to 100° from the center of the target, 6° to 90° from 200 mm upstream, and 10° to 120° from 200 mm downstream. The chamber was trapezoidal in shape to angle the windows forward to make more of the target cell "visible" to the 12° detectors.

In addition to windows, the chamber had ports for the beamline (up- and downstream), for pumping (on the bottom surface), and for access to

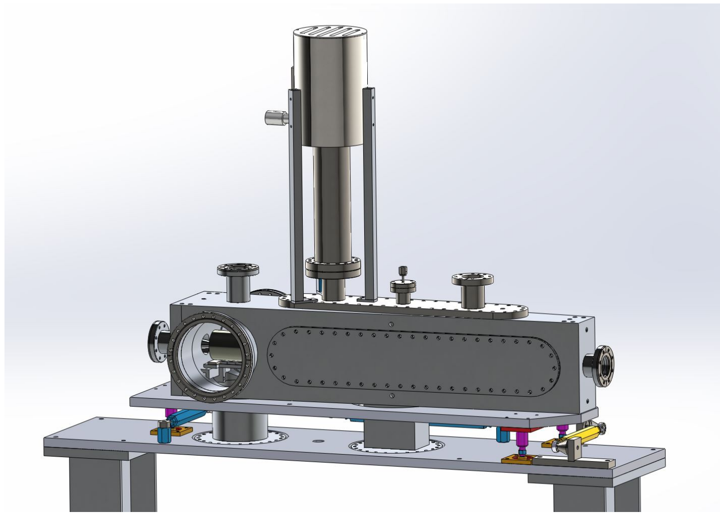

Fig. 4: CAD model of the OLYMPUS scattering chamber.

the collimator (on the left and right), as well as the target cell flange on the top, which had feedthroughs for the hydrogen gas, the coldhead, and various sensors. The main components inside the scattering chamber are shown in Fig. 5.

3.3. Wakefield Suppressors

Wakefield suppressors were necessary to maintain the target cell at cryogenic temperatures by preventing heating caused by wakefields. The wakefield suppressers consisted of conducting transitions that were added to fill gaps between conducting structures surrounding the beam. Any sharp transitions or gaps in conductivity would serve as electrical cavities that would be excited by the passing beam, creating wakefields and producing heat. To prevent this, three wakefield suppressors were produced to cover the following transitions:

1. from the circular upstream scattering chamber port (60 mm in diameter) to the 25 mm by 7 mm elliptical opening of the collimator,
2. from the exit of the collimator to the entrance of the target cell (both 27 mm by 9 mm ellipses), and
3. from the 27 mm by 9 mm elliptical exit of the target cell to the circular downstream scattering chamber port (60 mm in diameter).

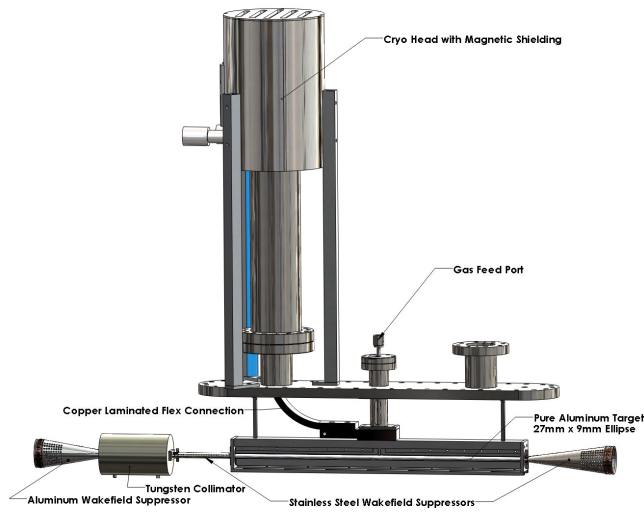

Fig. 5: CAD model of the target cell, wakefield suppressors, and collimator inside the OLYMPUS scattering chamber.

With these wakefield suppressors, a target temperature of around 50 K could be maintained during synchrotron operation, and a temperature less than 70 K could be maintained during high-luminosity OLYMPUS running.

The wakefield suppressors were made of stainless steel (except the upstream wakefield suppressor, which was made of aluminum), and plated with silver for improved electrical conductivity. The surfaces were smooth except for many small holes, which were drilled to allow the vacuum system to pump gas through them. The ends of the wakefield suppressors had beryllium-copper spring fingers around their circumference. These spring fingers made sliding connections at an interface that allowed for thermal expansion while maintaining good electrical contact. The upstream wakefield suppressor was screwed directly to the collimator, while making a sliding connection with the upstream scattering chamber port. The other two wakefield suppressors were fixed to rings clamped to the ends of the target, and made sliding connections to either the downstream scattering chamber port or the collimator. A close up view of the middle wakefield supressor is shown in Fig. 6.

3.4. Collimator

Fig. 6 also shows the fixed collimator in front of the target cell. The collimator consisted of a 139.7 mm long cylinder of tungsten 82.55 mm in

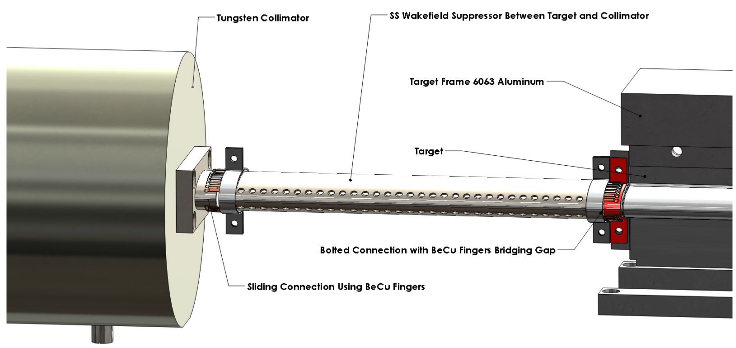

Fig. 6: CAD model of the wakefield suppressor between the collimator and the target cell.

diameter. The outer dimensions were chosen after performing a study on simulated showers of beam-halo particles. It had a tapered elliptical aperture with entrance 25 mm by 7 mm and exit 27 mm by 9 mm. The collimator was machined from a solid block of tungsten using wire electrical discharge machining, EDM[7]. The entrance dimensions were chosen to be slightly smaller than those of the storage cell to shield the target cell walls.

3.5. Vacuum System

A system of magnetic levitation turbomolecular pumps[8] (800 l/s capacity) and NEG pumps[9] (400 l/s capacity) were used to pump the section of beamline inside the OLYMPUS experiment. This system utilized three stages of pumping to reduce the pressure from the relatively high pressure ($\sim 10^{-6}$ Torr) at the scattering chamber (caused by hydrogen gas) to the low pressure ($\sim 10^{-9}$ Torr) of the DORIS storage ring.

The vacuum system is shown in Fig. 7. Six turbomolecular pumps (models Osaka TG 1100M and Edwards STP 1003C) formed a differential pumping system to prevent hydrogen in the target from contaminating the vacuum of the storage ring. Two turbo pumps located in the pit directly beneath the experiment were directly connected to the scattering chamber through 200 mm

[7]Jack's Machine Co. Hanson, MA 02341
[8]Osaka and Edwards
[9]SAES Capacitor CFF 4H0402

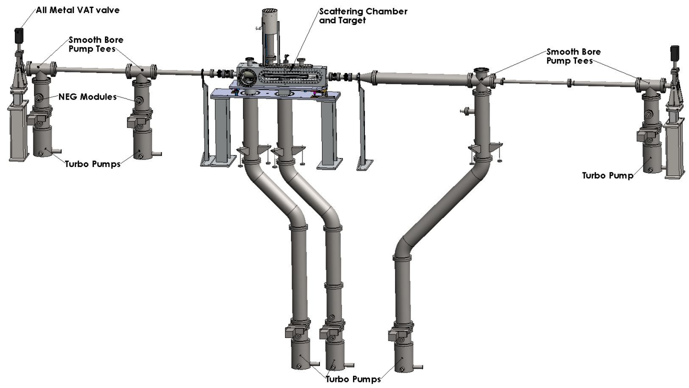

Fig. 7: CAD model of the vacuum system employed on the OLYMPUS experiment.

diameter pipes. Two more turbo pumps were connected to the up- and downstream beamlines approximately 2 m from the target. At approximately 3 m from the target another two turbo pumps were used to reduce the pressure in the beamline to the level acceptable for the DORIS storage ring. The four pumping stations furthest from the target also had NEG pumps to improve the pumping of hydrogen.

4. The OLYMPUS Detector

The core of the OLYMPUS detector consisted of components from the BLAST spectrometer from MIT-Bates (26). The toroidal magnet, time-of-flight detectors, and many of the readout and control electronics were shipped to DESY in Spring 2010. The components were reassembled, reconditioned, and modified as necessary for installation in OLYMPUS detector.

The OLYMPUS Experiment was installed in the straight section of the DORIS storage ring, in the location of the former ARGUS Experiment (25). The initial assembly took place from June, 2010 to July, 2011 outside of the DORIS tunnel, to avoid interferring with DORIS operation. The detector was assembled on a set of rails that led (through a removable shielding wall) to the ARGUS site. When the assembly was complete, the shielding wall was removed, the spectrometer was rolled into place in the tunnel, and the wall was rebuilt. The experimental site was 7 m wide, with a 5 m deep pit below the beam height. The pit was a convenient location for vacuum pumps, power supplies, and the target gas low system because it was deep enough to be outside of the fringes of the magnet field.

In the area outside the shielding wall was an electronics "hut," which was supported on the same set of rails. The hut housed the detectors' readout and control electronics, the high voltage supplies, and the computer systems, and could be accessed even when the DORIS beam was circulating.

The OLYMPUS spectrometer consisted of an eight-coil toroidal magnet with detector instrumentation in the two sectors of the horizontal plane of the beamline (see Fig. 8). Each of these sectors contained a large drift chamber for particle tracking and and array of time-of-flight scintillator bars for trigger timing and rough energy and particle position measurements. To monitor the luminosity, OLYMPUS had a redundant system of a Symmetric Møller/Bhabha (SYMB) calorimeter at $\theta = 1.29°$ and detector telescopes consisting of three triple gas electron multiplier (GEM) detectors interleaved with three multi-wire proportional chambers (MWPCs) at 12° in both sectors.

The following sections describe the detector components in greater detail.

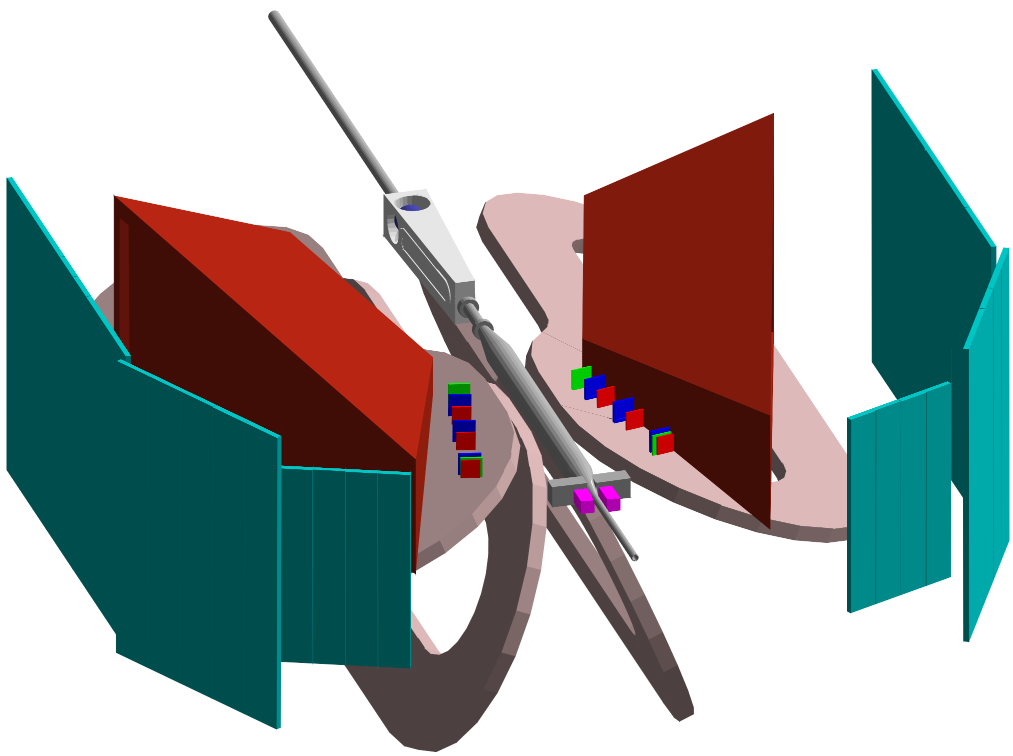

Fig. 8: A solid-model representation of the OLYMPUS detector with the top four magnet coils removed to show the instrumented horizontal sectors.

4.1. Toroidal Magnet

The toroidal magnet consisted of eight copper coils placed around the beam line and scattering chamber so that the beam traveled down the toroid's symmetry axis (see Fig. 9). The coils divided the space around the beamline

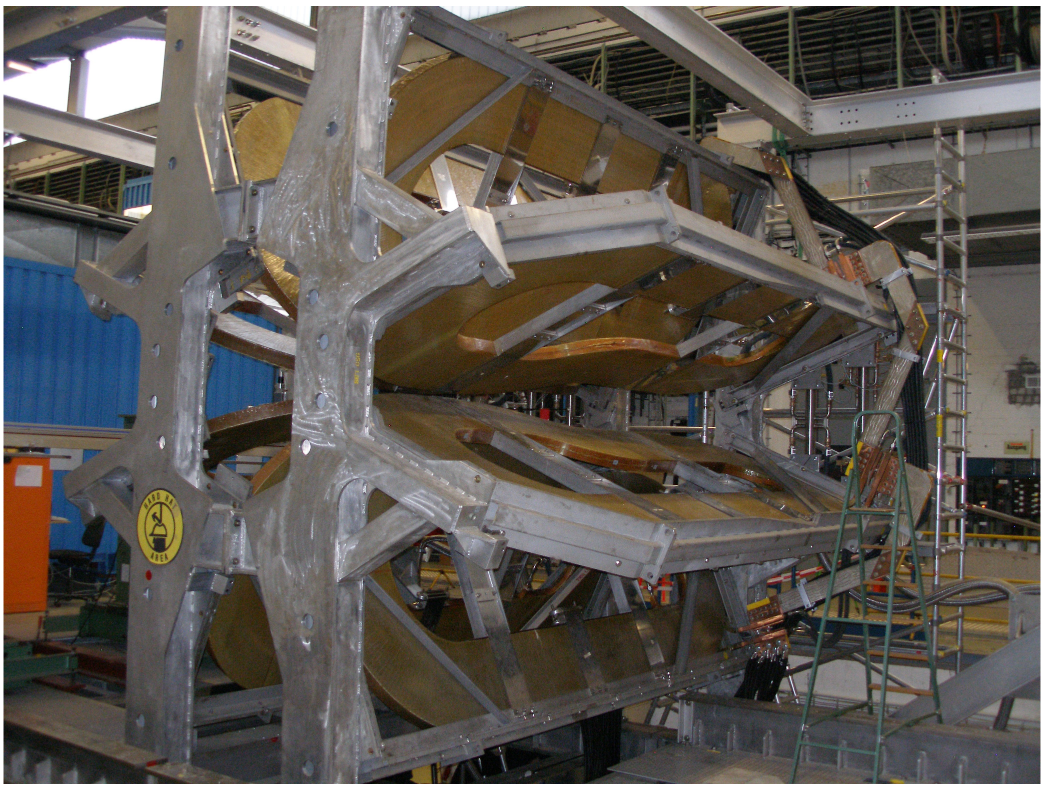

Fig. 9: The toroid magnet assembled at DESY before the subdetectors were installed

into eight sectors. The two sectors in the horizontal plane were instrumented with detectors. During normal operation, the magnet produced a field of about 0.28 T in the region of the tracking detectors.

The magnet was originally designed and used for the BLAST experiment, and has been described in a previous article (27). The choice of a toroidal configuration was made to ensure a small field along the beamline in order to minimize any effects on a spin-polarized beam and to limit field gradients in the region of the polarized target. Since OLYMPUS used neither a polarized beam nor a polarized target, these concerns were not as important. However, during the initial set-up, the magnetic field along the beamline was measured and the coil positions adjusted to achieve an integrated field < 0.005 T·m to avoid perturbing the beam's position or direction.

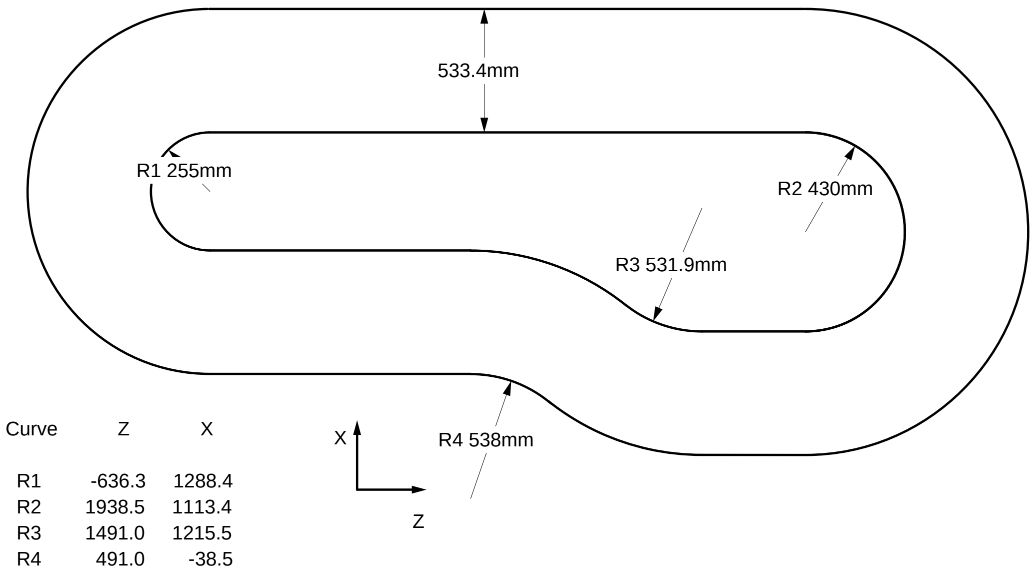

Fig. 10: Plan view of BLAST coil outline showing dimensions and position relative to the center of the target cell.

Each of the toroid's eight coils consisted of 26 turns of 1.5 inch square copper tubes, organized into two layers of 13 turns. A circular hole, 0.8 inches in diameter, ran down the length of each tube and served as a conduit for cooling water. During assembly, the tubes were individually wrapped with fiberglass tape and then collectively potted in an epoxy resin matrix. The final outline and nominal position relative to the beam line and target center at the coordinate origin are shown in Fig. 10. The coils are narrower at one end to accommodate the scattering chamber and wider at the other to extend the high-field region to more forward angles, where scattered particles have higher momenta.

The magnetic field served two purposes. The first was to bend the tracks of charged particles, allowing their momentum and charge sign to be determined from the curvature of their tracks. The second was to sweep away low-energy, charged background particles from the tracking detectors. Though a stronger magnetic field would have improved momentum resolution and reduced the background, it would also have increased the Lorentz angle of drift electrons in the tracking detectors, making track reconstruction more difficult. A balance was struck by choosing a current of 5000 A for normal operation, which produced a field of about 0.28 T in the high-field regions.

Originally, it was planned to alternate the polarity of the magnet every few hours to reduce systematic uncertainties. However, this proved impractical at high-luminosity. In the negative polarity setting, the magnet bent negatively charged particles outward from the beamline. The drift chambers were hit with large background of low-energy electrons, which frequently caused the high-voltage supply to exceed its current threshold and deactivate. Attempts to adequately shield the drift chambers, both by adding material and by increasing the magnetic field strength, were unsuccessful. Consequently, the negative polarity setting was limited to low-luminosity running, and only about 13 % of the total luminosity was collected in this mode. The limited negative polarity data will provide a check on systematic uncertainties.

After the experimental running period was completed, the drift chambers, the 12° luminosity monitors, the Møller detector, and the beamline downstream of the scattering chamber were removed in order to conduct a measurement of the magnetic field. The field region was scanned using a 3D Hall probe mounted to a rod, driven by several translation tables. The rod was mounted to a long XYZ table with a range of motion of 0.2 m by 0.2 m by 6 m. (By convention, the direction of the beam was labeled as the OLYMPUS Z-axis, the Y-axis pointed up, and the X-axis pointed toward the left sector, forming a right-handed coordinate system.) This long table was supported by two large XY tables that augmented the X and Y ranges each by 1 m. The range of motion was further extended in X by substituting rods of different lengths and in Y by adding a vertical extension piece. The apparatus was used to measure the field over a grid of points on the left sector, before being transported and reassembled for a similar measurement of points on the right sector. The grid extended from -0.5 m to 3.5 m in Z. In X and Y, the grid was limited to the triangular space between the coils, but extended to $\pm$2.7 m on either side of the beamline. The grid points were spaced 0.05 m apart in the region within 1 m of the beamline, and 0.10 m apart in the outer region, where the field changed less rapidly. In total, approximately 35,000 positions were measured, including the downstream beamline region, which was measured redundantly from the left and the right.

After the initial setup of the apparatus, the precise position of the XYZ tables was measured with a laser tracking station over the course of a typical scan in Z. This showed that the Hall probe position varied in X and Y as a function of Z during a scan, but that the shape was quite reproducible. To correct for this variation, the start and end points of each scan were measured using a theodolite and a total station. This data then allowed the position of the Hall probe to be determined for each measurement.

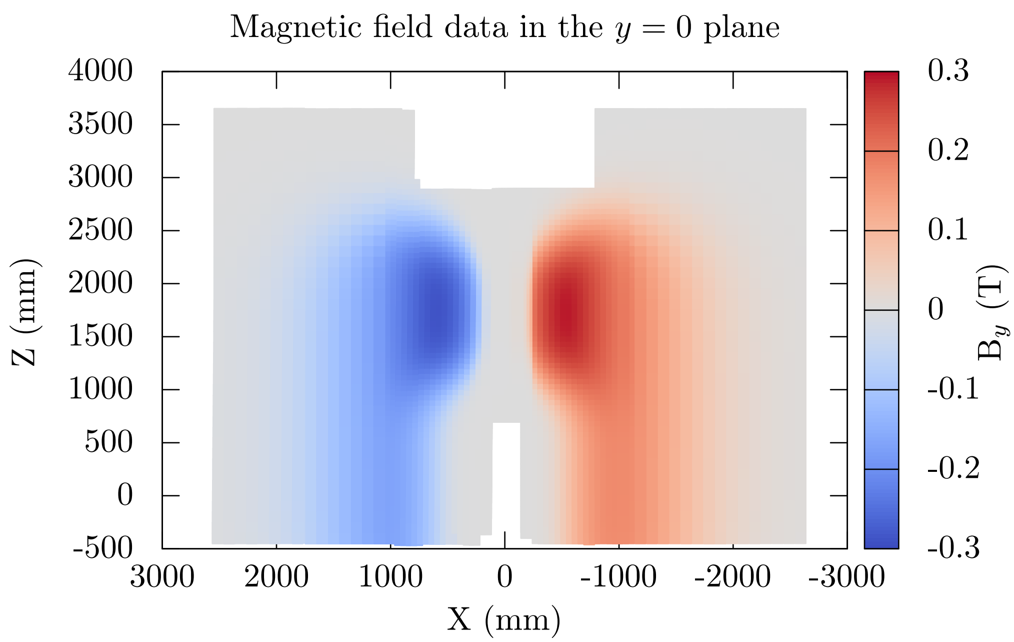

Fig. 11: The data from the magnetic field measurements in horizontal plane as viewed from above

After correcting the Hall probe positions, a fit was performed to the magnetic field data. The fit was based on a model of the coil geometry with a Biot-Savart calculation of the magnetic field. The fit allowed the coil positions to vary slightly to best match the measurements. This model was then used to extrapolate the field over the entire volume around the OLYMPUS detector for use in track reconstruction and in the OLYMPUS Monte Carlo simulation.

4.2. Drift Chambers

The drift chambers used for the OLYMPUS experiment came from the BLAST experiment at MIT-Bates and have been described in great detail elsewhere (26), so the following description will be brief while mentioning new and updated features.

The drift chambers were used to measure the momenta, charges, scattering angles, and vertices of out-going charged particles. This was achieved by tracking those particles in three dimensions through the drift chambers, which were positioned within the toroidal magnetic field. Reconstructing a particle's trajectory backwards to the scattering vertex allowed the scattering angles and vertex position to be determined. Measuring the curvature of a trajectory yielded the particle's momentum, while the direction of curvature indicated the sign of particle's charge. The drift chambers had a large angular acceptance and nominally subtended a range of 20°–80° in polar angle and a ±15° range in azimuth. The chambers were oriented to be normal to a polar angle of 73.54°. Because of these choices, the chambers were trapezoidal in shape (see Fig. 12).

The drift chambers were arranged in two sectors that were positioned on either side of the target, in the horizontal plane. Each sector contained three drift chambers (inner, middle, and outer) joined together by two interconnecting sections to form a single gas volume. Thus, only one entrance and one exit window were needed, reducing multiple scattering and energy loss. A cross sectional view of the top plate of one of the assembled gas volumes is shown in Fig. 13. The drift chambers combined had approximately 10,000 wires, which were used to create the drift field. Of these, 954 were sense wires, which read out the signals from ionization caused by a charged particle track.

Each chamber consisted of two super-layers (or rows) of drift cells, with 20 mm separation between the super-layers. The drift cells were formed by wires in a "jet style" configuration. Fig. 14 shows a cross-sectional view of a portion of one chamber with the two super-layers of drift cells. It also shows characteristic "jet-style" lines of electron drift in a magnetic field. Each drift cell was 78×40 mm^2 and had 3 sense wires staggered ± 0.5 mm from the center line of each cell to help resolve the left/right ambiguity in determining position from the drift time. The wires in one super-layer were strung with a 10° stereo angle relative to wires of the other so that each chamber could localize a trajectory in three dimensions.

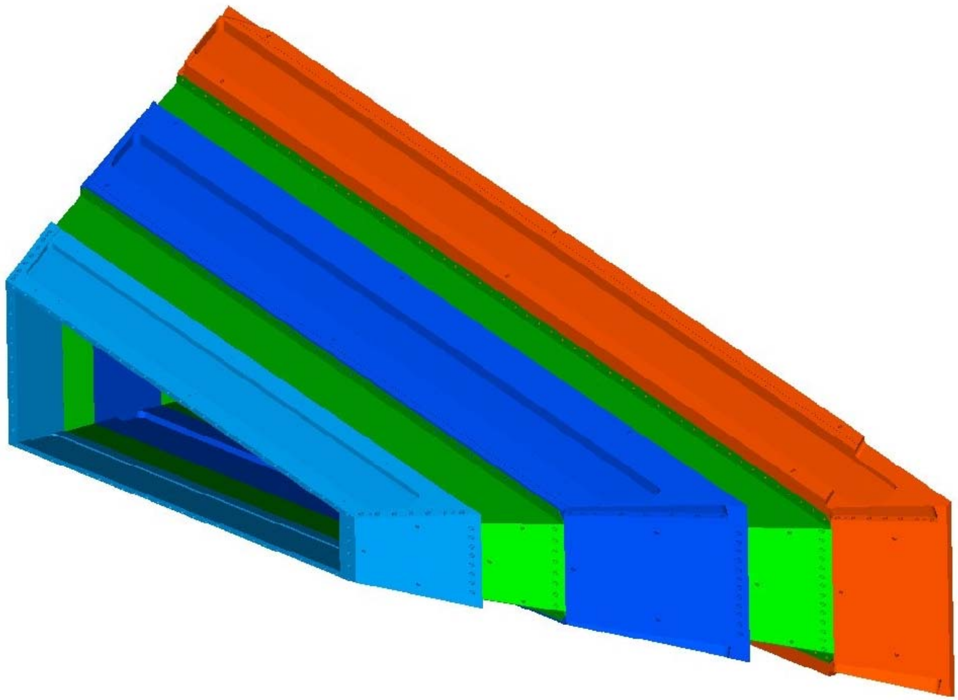

Fig. 12: Isometric view of all three drift chambers assembled into a single gas volume.

Because transporting the chambers in a way that would protect the wires from breaking was infeasible, the chambers were unstrung before being shipped from MIT-Bates to DESY. The chambers were then completely rewired in a clean room at DESY over a period of about three months during the summer of 2010. In addition to new wires, improvements were made to the front-end electronics, building on experience gained from BLAST.

For the experiment, an Ar:CO_2:C_2H_6O gas mixture ($87.4 : 9.7 : 2.9$) was chosen for the drift chambers. The ethanol was added by bubbling a Ar:CO_2 ($90 : 10$) gas mixture through a volume of liquid ethanol kept at $\sim 5°$C. The chambers were maintained at a pressure of approximately 1 inch of water above atmospheric pressure with a flow rate of around 5 L/min.

Signals in the sense wires were processed with front-end electronics housed in the recesses of the interconnecting sections before being sent to TDC modules in the electronics hut. The signals were first decoupled from the high-voltage on new, custom-designed, high-voltage distribution boards. The sig-

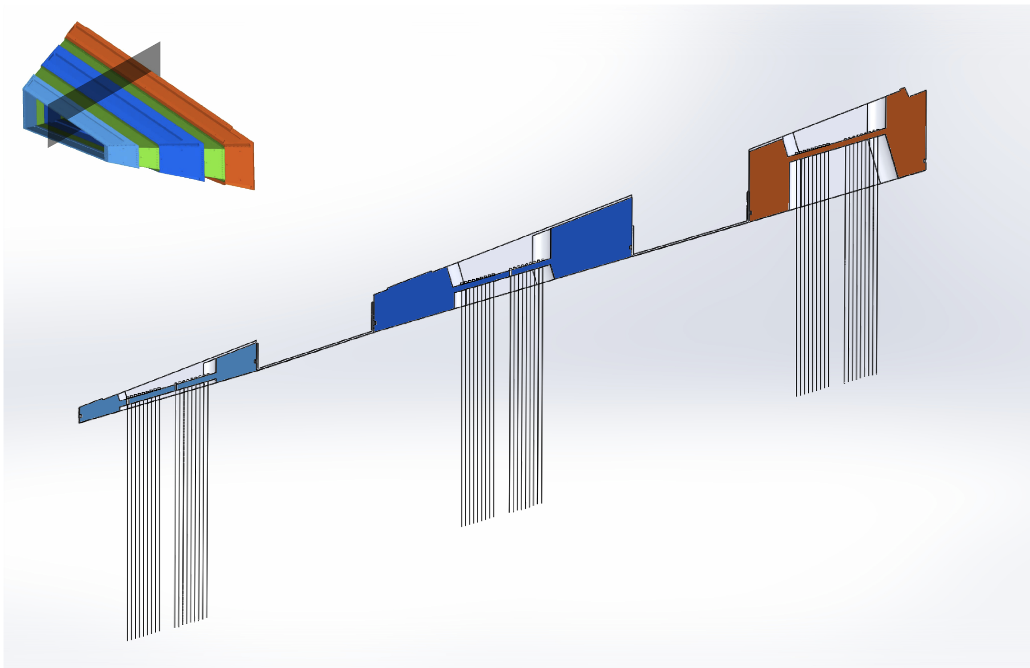

Fig. 13: Cross sectional view of the top plates of the three drift chambers and the two interconnecting sections when assembled into a single gas volume. The recesses between the top plates of the individual chambers housed front-end electronics and cables.

nals next passed to Nanometrics Systems[10] N-277L amplifier/discriminators. Then the signals were passed by Ethernet cable to the electronics hut, to LeCroy[11] 1877 Multihit TDC modules, operated in common-stop mode, with the stop signal being provided by a delayed trigger signal. The digitized signals were read out by the data acquisition system. An example TDC spectrum for a single wire is shown in Fig. 15.

[10]Nanometric Systems, Berwyn, IL, USA
[11]Teledyne Lecroy, Chestnut Ridge, NY, USA

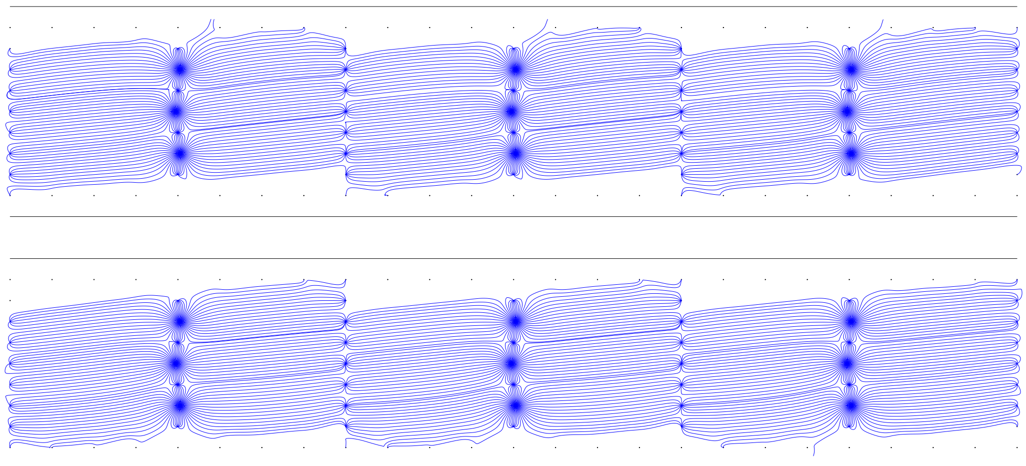

Fig. 14: Portion of a chamber showing the two super-layers of drift cells formed by wires. Lines of electron drift in the drift cells assuming a typical magnetic field around 3.0 kG are also shown.

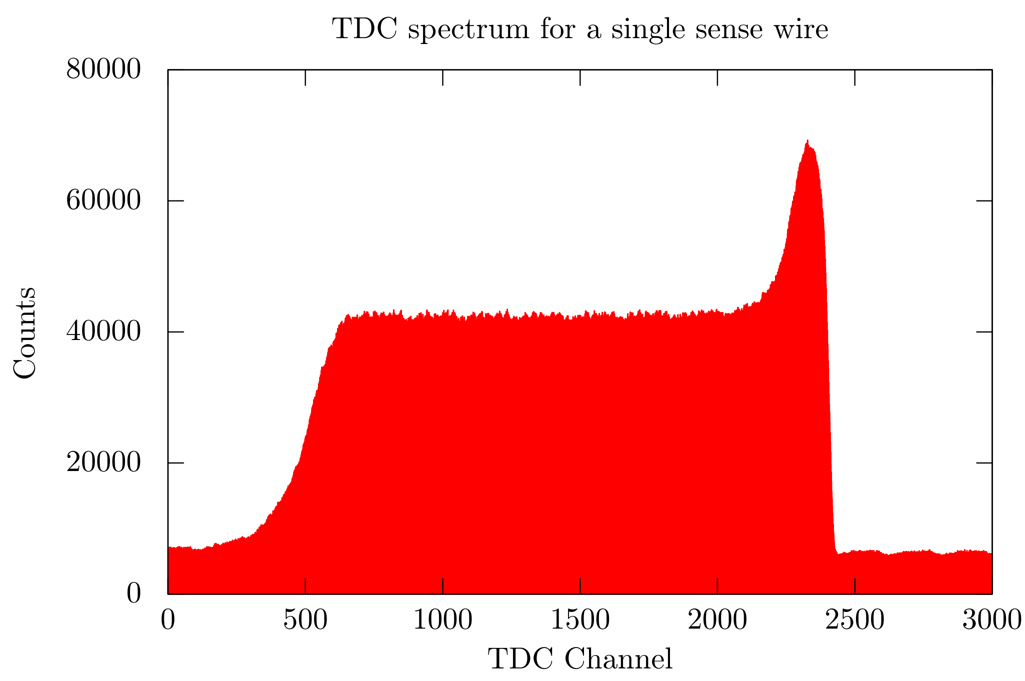

Fig. 15: A typical TDC spectrum for a single wire has a "church shape," which is characteristic of jet-style drift chambers in common stop mode.

4.3. Time of Flight Detectors

The time-of-flight (ToF) detector was adapted from the system used for the BLAST Experiment (26). Each sector consisted of 18 vertical scintillator bars read out with photo-multiplier tubes (PMT) mounted at both ends, as shown in Fig. 16. The four most-forward bars on each side were 119.4 cm high, 15.2 cm wide, and 2.54 cm thick. The remaining 14 bars on each side were 180.0 cm high, 26.2 cm wide, and 2.54 cm thick, so as to cover the entire acceptance of the drift chambers. The Glasgow University group designed and constructed a new support structure which allowed a tight arrangement and quick replacement of individual bars. The bars were arranged in three planar sections oriented with their normal approximately pointing toward the target area.

The ToF detector provided the timing signals used to trigger the readout and data acquisition system for the majority of detector components. In particular, it provided the common stop signal for the drift chamber TDCs. The main trigger logic of the experiment required presence of at least one

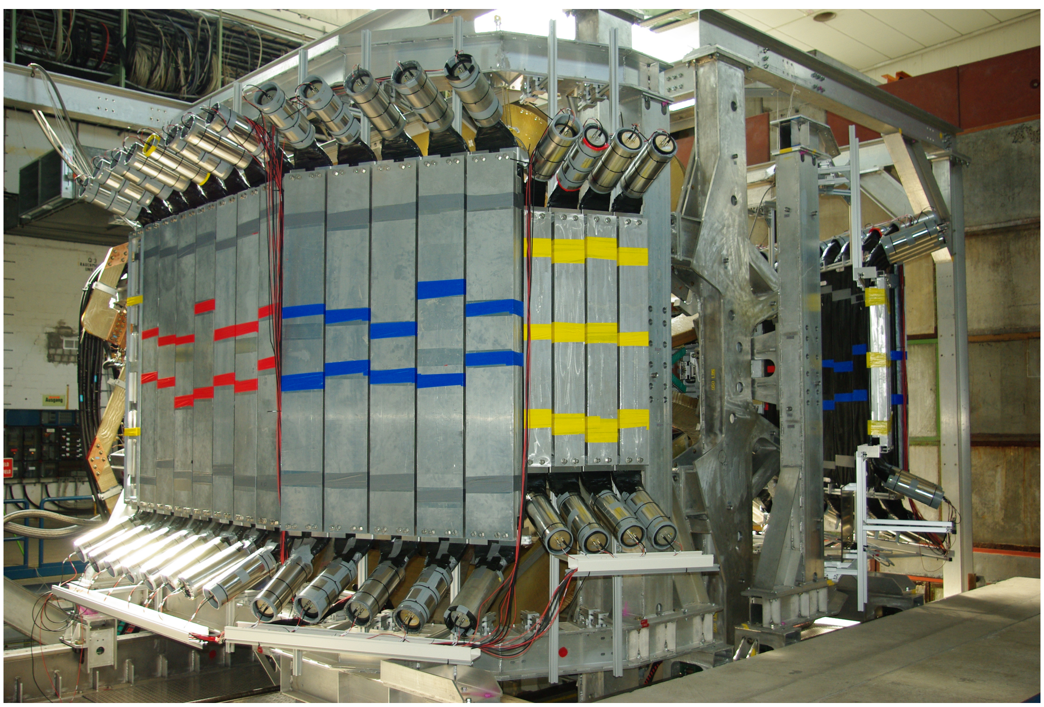

Fig. 16: Photograph of the mounted ToF detectors during OLYMPUS assembly of the OLYMPUS detector.

top/bottom ToF PMT coincidence in both sectors (see Sec. 6). The ToF PMT signals were processed through passive splitters and recorded by both TDCs and ADCs. The signals from the analog output were discriminated with constant fraction discriminators (CFD) and the logic signals were further processed for the trigger, to start the individual ToF TDC, and to generate the common stop signal for all TDCs. The rearmost two bars in each sector were not present in BLAST, and were added to expand the acceptance of OLYMPUS at large θ. Their signals were processed with leading-edge (LE) discriminators. The differential splitter outputs were connected to the ADCs for signal integration. The integrated ADC signal from a given bar provided an estimate of the energy deposited in the bar, while the relative time difference between the top and bottom tube signals from a bar provided a rough measurement of the hit position. The mean signal times of the top and bottom signals were approximately independent of the hit position. Mean times between pairs of ToF bars in both sectors provided measurements of the time-of-flight of cosmic ray particles and of the difference in time-of-flight between the scattered and recoiling particle from interactions in the target.

The active volume of the ToF bars consisted of Bicron[12] BC-408 plastic scintillator, chosen for its fast response time (0.9 ns rise time) and long attenuation length (210 cm). At the ends of each bar, the sensitive volumes were connected via Lucite light guides to 3-inch diameter Electron Tubes[13] model 9822B02 photomultiplier tubes equipped with Electron Tubes EBA-01 bases. The PMT signals exhibited a typical amplitude of ~ 0.8 V with a rise time of a few ns. The light guides were bent away from the interaction region so as to orient the PMTs roughly perpendicular to the toroidal magnetic field. Additionally, each PMT was encased with μ-metal shielding. Due to these measures, the toroidal magnetic field had no discernible effect on the ToF gains. Each PMT base utilized actively-stabilized voltage dividers to avoid variation of signal timing with gain.

Due to aging and radiation damage of the bars, somewhat smaller attenuation lengths of 120-180 cm were found from the analysis of TDC and ADC signals, shown in Fig. 17. Some of the bars showed advanced opaqueness and were replaced before data taking. The level of degradation of the remaining bars was still tolerable and did not adversely affect the ToF performance.

[12]Bicron, Solon, OH, USA
[13]Electron Tubes Ltd, Ruislip, Middlesex, England

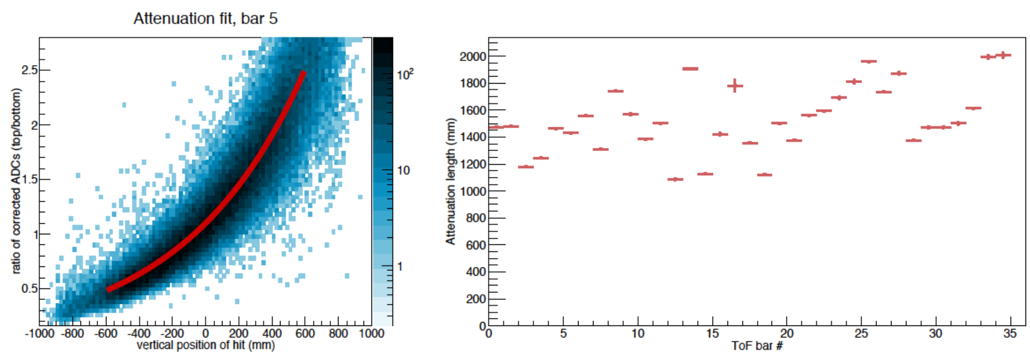

Fig. 17: A sample fit to the TDC and ADC data from a single bar to produce an estimate of the attenuation length for the bar (left) and the results of this fit for all bars (right).

The efficiencies for top/bottom coincidences were measured by sandwiching each bar with a pair of small test scintillators and were found to be around 98-99% for signals registered near the center of the bar. Additional ToF efficiency estimates were conducted by evaluating events with minimum trigger bias.

5. Luminosity Monitors

In order to measure the ratio of differential cross sections for positron-proton and electron-proton elastic scattering, it was essential to monitor the luminosity for each run very precisely. In particular, the physics goals of OLYMPUS required the very precise and accurate measurement of the ratio of the integrated luminosities with positron and electron beams delivered to the experiment. OLYMPUS required a system in which individual measurements of the instantaneous luminosity were made with sufficient statistical precision and over sufficiently small time scales so as to eliminate effects from any slowly varying parameters that affect the response of the detectors. To achieve this, OLYMPUS included three systems to measure the luminosity redundantly:

- The slow control system (Sec. 8) monitored the beam current and gas flow to the target. The system additionally used measurements of the target cell temperature, in conjunction with the known cell geometry, to compute the target density and thickness during running. The product of the target thickness and beam current was integrated and corrected for the deadtime of the data acquisition system over a run produced an approximate first estimate of the integrated luminosity of a data run.

- The 12° luminosity monitors (Sec. 5.1) measured elastically scattered leptons over a small angular range around $\theta \approx 12^\circ$ in coincidence with the recoil proton in the rear of the opposite sector drift chamber. Each monitor consisted of a telescope of three triple gas electron multiplier (GEM) detectors (Sec. 5.1.1) interleaved with three multi-wire proportional chambers (MWPCs) (Sec. 5.1.2). Since at $\theta = 12^\circ$ the two-photon contribution to elastic scattering is expected to be negligible, the known *ep* elastic cross section at this angle can be used to provide a beam species independent luminosity measurement. The 12° system was designed to measure the luminosity with statistical precision better than 1% per hour.

- A high precision measurement using symmetric Møller and Bhabha scattering was implemented using PbF_2 calorimeters placed symmetrically at $\theta = 1.292^\circ$ in the left and right sectors (Sec. 5.2). Comparing the observed e^-e^- and e^+e^- elastic scattering rates with the known Møller and Bhabha cross sections provided a measure of the luminosity for each beam species with the very high statistical precision in very short time frames.

The implementations of the 12° and symmetric Møller/Bhabha luminosity monitoring systems are discussed in detail in the immediately following sections, while Fig. 18 provides a schematic overview of these systems.

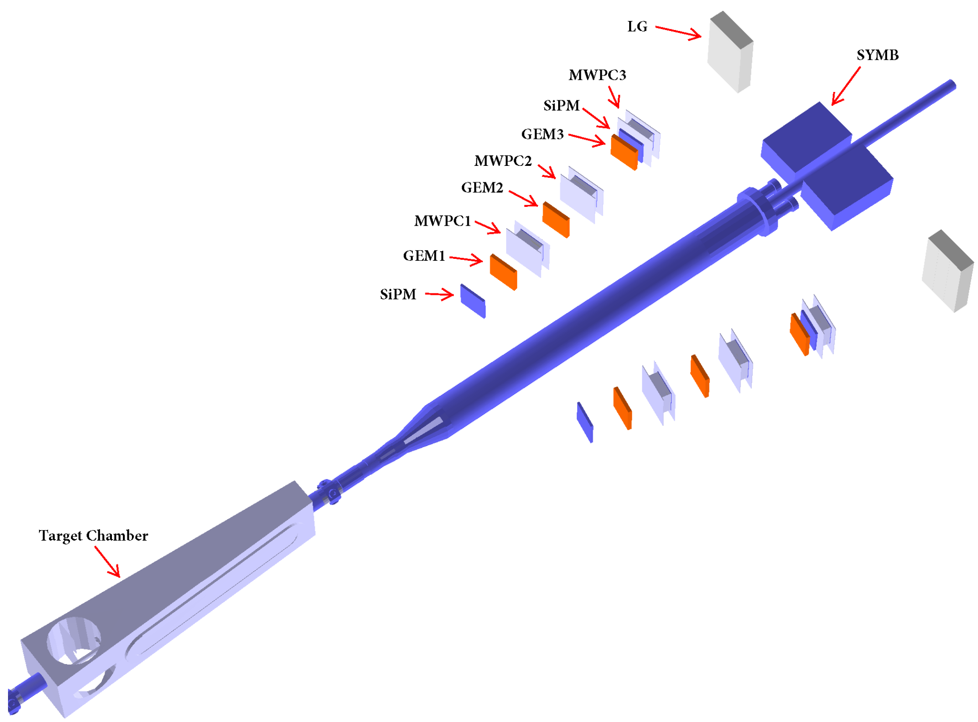

Fig. 18: Overview of the luminosity monitoring systems based on elastic ep scattering at $\theta = 12°$ (GEM/MWPC) and symmetric Møller/Bhabha scattering (SYMB calorimeter).

5.1. *The* 12° *Luminosity Monitoring System*

The 12° luminosity monitoring system consisted of two telescopes each composed of three triple-GEM and three MWPC elements, triggered by a pair of thin scintillators with silicon photomultiplier (SiPM) readout. There were several considerations which drove the design of the 12° system. The detector elements were desired be low mass and with an active area of about 10×10 cm^2, corresponding to an approximate solid angle of 1.2 msr at a maximum distance of about 2.9 m from the target. The detector acted as a tracking telescope covering a range of the small lepton scattering angle region where the asymmetry between electron and positron scattering was expected to be negligible. The telescopes fit in the forward cones between the pairs of toroid coils on each side of the beamline with a clear view of the scattering chamber window and cell. While the telescopes were initially designed with only the three GEM layers, the design for the MWPCs ultimately used was already available and was accommodated to provide an additional independent monitor. A picture of such a telescope in shown in Fig. 19.

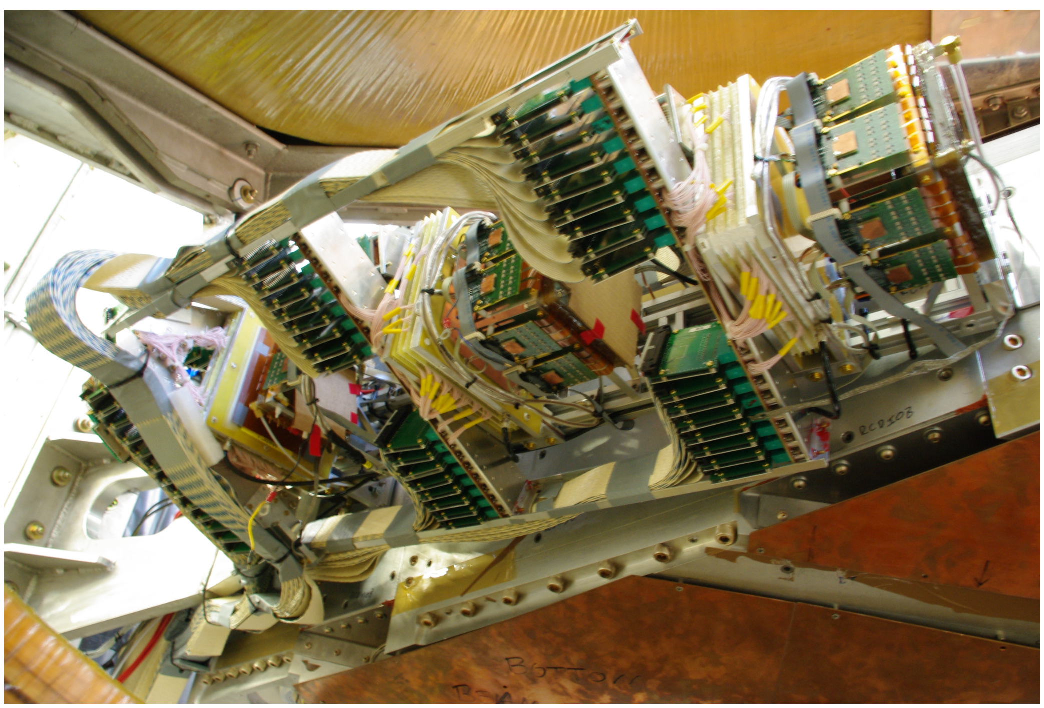

Fig. 19: Photograph of one of the 12° GEM/MWPC telescopes.

The readout for each telescope was triggered with pairs of thin scintillators in each arm in coincidence with the signal from the recoil proton registered in the rear ToFs of the opposite sector. With the chosen design, the monitoring rate guaranteed a statistical precision better than 1% per hour at the design luminosity of 2×10^{33} cm^{-2}·s^{-1}. The design was a trade-off between the resolution and total detector acceptance and the smallness of scattering angle in order to maximize the elastic count while minimizing the possible asymmetry between e^+ and e^- scattering due to two photon exchange.

5.1.1. 12° *GEM Detectors*

Six planar triple-GEM detectors with 2D strip readout were constructed at Hampton University and installed in sets of three on either side of the experiment to form telescopes aligned along $\theta = 12°$ relative to the beamline. The GEM detectors were designed at the MIT Bates Linear Accelerator Center. Six GEM chambers were installed, interleaved with the 12° MWPCs and trigger scintillators, and mounted on an integrated support structure attached to the forward face of the large drift chambers.

The detector was designed to utilize front-end electronics and readout cards designed and built by INFN Rome. MIT's experience designing and constructing large area GEM detectors for the Forward GEM Tracker (FGT) upgrade to STAR at RHIC (28) also provided design insight to make the detector easy to construct and robust.

Each individual GEM chamber was constructed as a stack of frames and foils glued together (see Fig. 20). Each stack included a readout board with three GEM foils and a cathode foil above the active area. Two pressure volume foils formed the outermost layers of the stack. There was a 2 mm space between each GEM foil and between the last GEM foil and the readout board. The pressure volume foils and the high voltage foils were spaced 3 mm from the adjacent foils. All of the components were tested individually before they were assembled into a detector. All of the electrical and gas connections were accessible on the edges of the stack, or in special cut outs in the case of the high voltage connections. A simple resistive voltage divider card provided the high voltage to all foils. A standard non-flammable premixed gas of Ar:CO_2 70:30 was used for the detector volume.

The GEM foil, cathode, and readout foils were manufactured by TechEtch

Inc. in Plymouth, MA[14]. Each GEM foil consisted of 50 μm thick Kapton clad on both sides with 5 μm thick layers of copper. The GEM foils were perforated with 70 μm holes at a 140 μm pitch over the entire area of the detector (approximately 10×10 cm^2). A special cathode foil was made of a piece of 50 μm Kapton layer with a 5 μm copper layer on only one side and no holes to provide a uniform electric field throughout the primary ionization area. Pressure volume foils on top of the cathode foil and below the readout foil prevented the gas pressure inside the detector from deforming the readout foil or the cathode foil. The pressure volume foils consisted of 50 μm thick aluminized Mylar, which additionally served to electrically shield the detector. The readout foil consisted of a 50 μm thick Kapton substrate foil. On the charge collection side of the foil there were precisely spaced pads and lines of 0.5-1.0 oz. (18-35 μm) gold-plated copper. The lines aligned

[14]http://www.tech-etch.com/

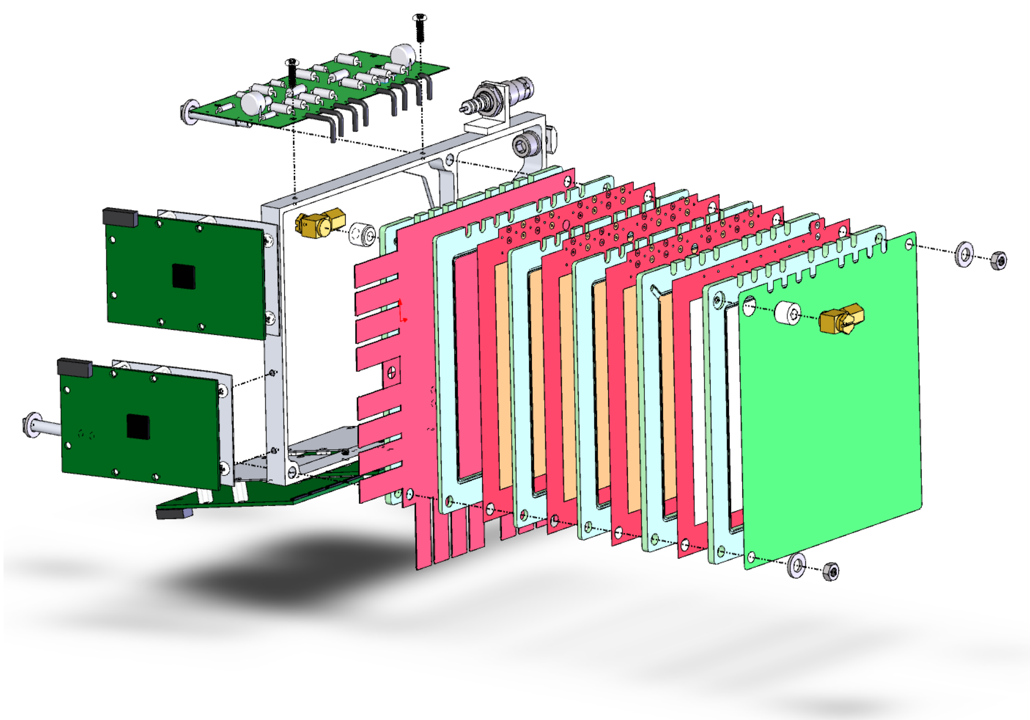

Fig. 20: An exploded view of a single triple-GEM detector.

vertically provided the horizontal coordinate of a hit. The pads were each connected with a via to the backside of the foil where they were connected to form rows to measure the vertical coordinate of a hit. The lines were 124 μm wide, at a 400 μm pitch. The pads were 124×323 μm^2, and also arranged at a 400 μm pitch. The spacing between the pads and the lines was 76 μm, and 70 μm between adjacent pads. The geometry was chosen such that the charge collected with the readout layer would be approximately equally shared between the horizontal and vertical readout channels.

The signals from the lines and pads were routed to two edges of the foil where they terminated on sixteen small arrays of pads designed to fit a flexible circuit connector, which was mounted on the front-end electronics card. Each card had four connectors (two cards per coordinate) corresponding to a total of four cards per GEM detector. Each GEM detector had 500 channels (250 per coordinate), with a total of 3000 readout channels for the GEMs in both telescopes. The front-end readout card designed by INFN Rome used one APV25-S1 analog pipeline chip per card (29). Each chip had 128 channels, each of which had a 192 cell analog pipeline which sampled the input channels at 40 MHz. Data were read out of the pipeline after a trigger event. All 128 channels were multiplexed onto a single data line which then ran to the DAQ system. The communication between the APV card and the DAQ system was maintained by a VME based control module hosting a field-programmable gate array (FPGA).

The finished detectors were mounted on an aluminum mounting bracket attached to the mounting rails that also held the MWPCs. The mounting bracket had flexible supports for the high voltage card and for the front end electronics cards. These allowed the positions of the cards to be adjusted during installation to avoid interference between components. Both the mounting bracket and the mounting rails were adjustable. Fiducials located on the GEM chambers allowed for precise surveying of the detector positions after the mounting was adjusted.

A charged particle traversing the GEM elements produced a charge cluster which was registered by several strips in both the vertical and horizontal directions. The reconstructed location of the clusters in x and y gave the spatial location of the particle as it passed through the detector. Digitization of the signal amplitudes of all channels allowed the detector to achieve high spatial resolution using centroid analysis. Intrinsic resolutions of approximately 70 μm have been achieved. The efficiency of each GEM detector was measured with candidate tracks based on the other five telescope elements and were found to be around 95% for all GEM elements.

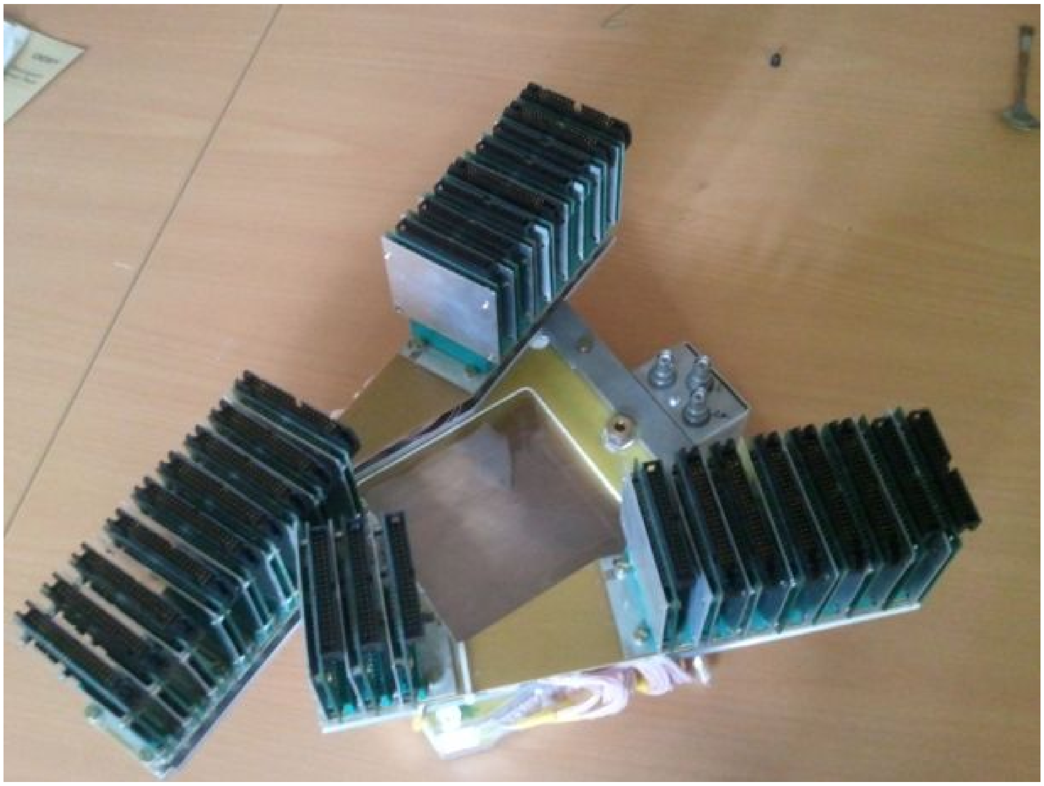

Fig. 21: Photograph of one MWPC with CROS3 readout electronics.

5.1.2. 12° *Multi-Wire Proportional Chambers*

Six identical MWPC modules, along with their CROS3 readout electronics (30), were fabricated at PNPI for the 12° luminosity telescopes. Three MWPCs were deployed in each telescope arm, as shown in Fig. 18. The readout cards for each module were arranged in two stacks around the active area, and are shown in Fig. 21.

The stacks were angled so that they could fit in the narrow space between the coils of the toroid.

Each MWPC module consisted of three planes of anode sense wires interleaved with cathode wire planes. The sense wires were made of gold-plated tungsten, had a diameter of 25 μm, and 1 mm separation. The cathode wires were made of beryllium bronze, with a diameter of 90 μm, and a separation of 0.5 mm. Each plane of wires had its own fiberglass frame. The module was assembled by sandwiching the planes together in a 10 mm aluminum outer frame. The three anode planes, labelled X, U, and V, had different orientations in order to measure a two-dimensional hit position. The U and V planes were angled by $\pm 30^\circ$ relative to the X plane, whose wires were vertical. Various parameters for the MWPCs are presented in Table 1.

Active area	112×112 mm^2
External dimensions	$180 \times 180 \times 50$ mm^3
Anode planes	X (0°), U ($+30^\circ$) and V (-30°)
Gap between anode and cathode	L=2.5 mm
Sense wire spacing	S=1 mm
Cathode wire spacing	S_{cath}=0.5 mm
Sense wire diameter	D=0.025 mm Au-plated tungsten
Cathode wire diameter	D_{cath}= 0.090 mm beryllium bronze
U, V angle wrt X wire	$\pm 30^\circ$
MWPC material in acceptance	$\sim 0.25\%$
Working gas mixture	65%Ar+30%CO_2+5%CF_4
Gas gain at work point	$\sim 7 \times 10^4$

Table 1: Working parameters of the MWPC modules

A gas mixture of 65%Ar+30%CO_2+5%CF_4 was chosen for the MWPCs based on the experience gained from the proportional chambers produced at PNPI for the HERMES Experiment (31). According to calculations using the program GARFIELD (32), this mixture would produce a gas gain of 7×10^4 in the MWPCs at the preliminary operating voltage of 3150 V. The operating voltage was chosen to be 3200 V after testing the MWPCs with a ^{55}Fe radioactive source. This operating voltage was validated by efficiency measurements during running conditions, where an efficiency of 98–99% was typically seen for all MWPC modules. Hit distributions for each plane, taken during the experiment are presented in Fig. 23.

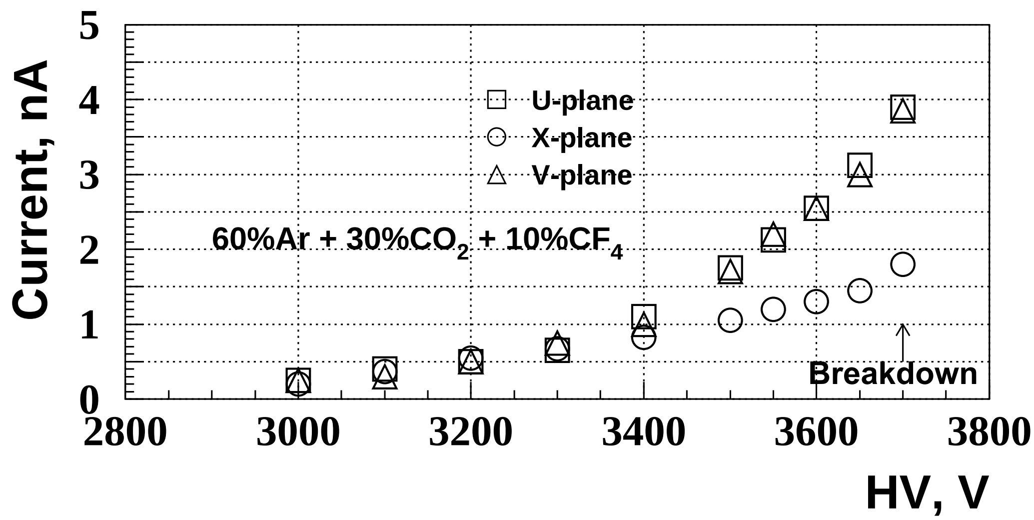

Fig. 22: Measured current on one MWPC from a ^{55}Fe radioactive source

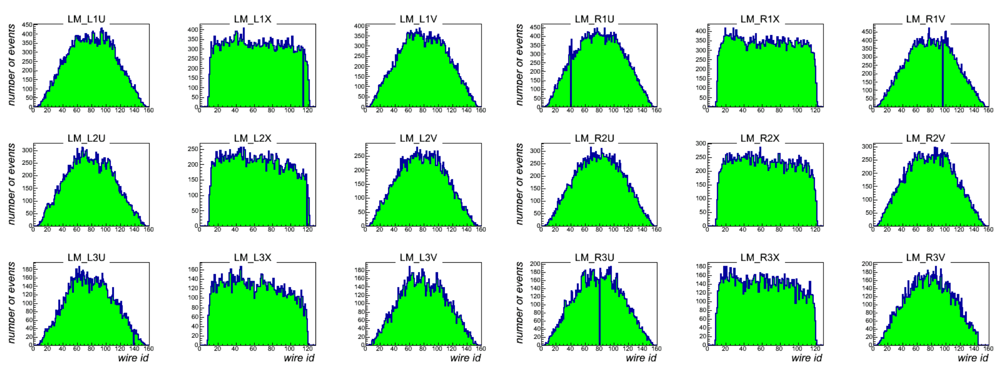

(a) Left MWPC telescope

(b) Right MWPC telescope

Fig. 23: Hit distributions for the left and right MWPC telescopes showing the XUV planes for the three detectors; one can see that just a few channels were lost because of the contact imperfections in the cards' connectors.

5.1.3. 12° *Trigger*

Each 12° telescope included two $120 \times 120 \times 4$ mm^3 scintillator tiles (Eljen EJ-204) to provide a trigger signal for the GEMs and MWPCs. Each scintillator tile was wrapped in Millipore Immobilon-P diffuse reflectors and read-out using two Hamamatsu multi-pixel silicon photomultipliers (MPPC) mounted on opposite corners of the tiles. This ensured a very high homogeneity of the light yield from the entire area of the tiles. The analog signals from each MPPC were summed and constant fraction discriminators provided the output signal from each tile. The trigger for reading out the 12° telescope on a given side consisted of the triple coincidence of the the two tiles on that side in conjunction with a trigger from a ToF bar in the rear region of the opposite side of the detector.

Additionally, lead glass calorimeters mounted behind the 12° telescopes in each section provided an independent means of triggering the detectors. Each calorimeter consisted of three lead glass bars attached to a PMT for readout. The additional trigger contributed the ability to measure the efficiency of the tile trigger continuously throughout data taking. The scintillator tiles exhibited efficiencies well in excess of 99% throughout the entirety of the experimental run.

5.2. *Symmetric Møller/Bhabha Luminosity Monitor*

The symmetric Møller/Bhabha scattering luminosity monitor (SYMB) monitored the luminosity delivered to the OLYMPUS experiment by measuring symmetric lepton-lepton scattering from the target. The scattering processes monitored consisted of Møller scattering ($e^-e^- \rightarrow e^-e^-$) in the case of electron beam running and Bhabha scattering plus annihilation to two photons ($e^+e^- \rightarrow e^+e^-$ and $e^+e^- \rightarrow \gamma\gamma$) in the case of positron beam running. At the OLYMPUS beam energy of 2.01 GeV, symmetric scattering occurred at a polar angle of 1.292° with respect to the beam direction (see Fig. 24 and **??**).

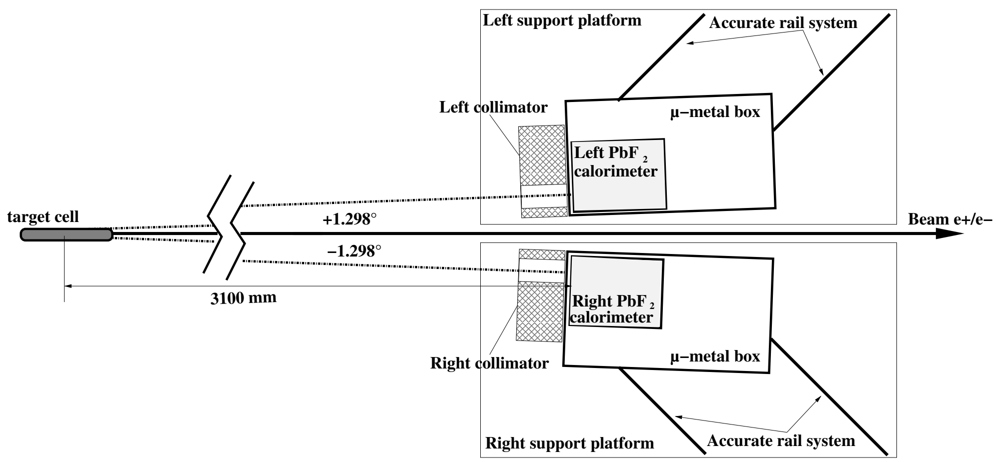

Fig. 24: A schematic of the Symmetric Møller/Bhabha luminosity detector (SYMB) showing the symmetric design about the beamline.

The detector provided a means measuring the luminosity with high precision by using the fact that the cross sections are precisely calculable from quantum electrodynamics and that the rates for symmetric lepton scattering are quite high. The identification of the symmetric coincidence of the reaction products in combination with the very high statistics of the measurement provided a means of determining the relative luminosity of electrons and positrons delivered to the experiment with the necessary precision for the OLYMPUS physics goals.

The SYMB, constructed at Johannes Gutenberg Universität in Mainz, Germany, consisted of two symmetric 3×3 arrays of lead fluoride (PbF_2)

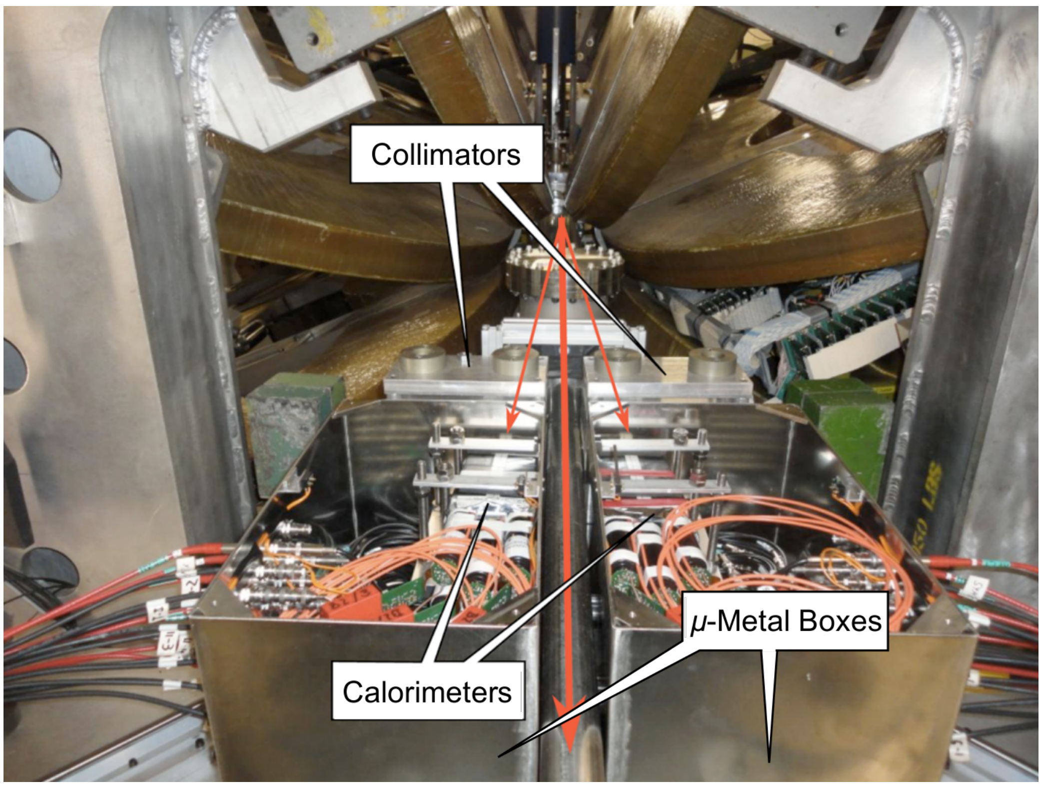

Fig. 25: A photograph showing the main components of the SYMB detector. The thick red line indicates the direction of the beam while the thinner red lines indicate the general path of scattered electrons, positrons, or photons entering the SYMB.

crystals, as shown in Fig. 26. A Philips XP 29000/01 PMT was connected to

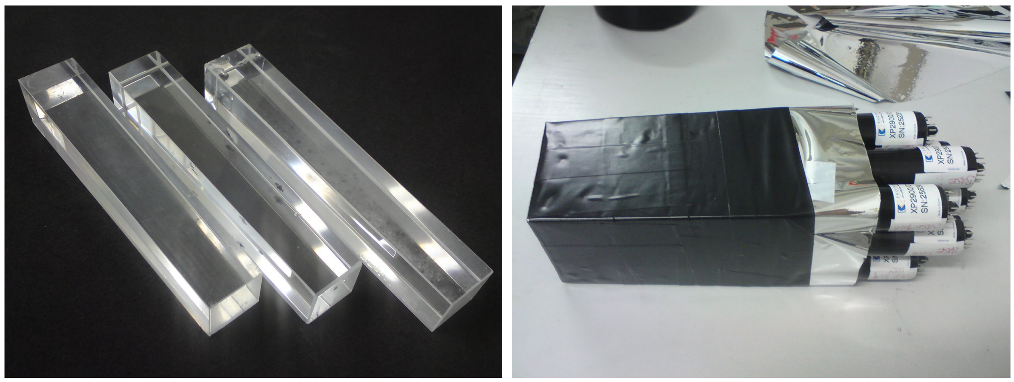

Fig. 26: Several of the PbF_2 crystals used in symmetric Møller/Bhabha luminosity monitor before (left) and after (right) assembly with the PMT readout system.

the end of each crystal to provide readout. Each crystal was approximately 26 mm×26 mm×160 mm, with a slightly tapered shape. The array of crystals on each side corresponded to approximately 17 radiation lengths and 2.17 Molière radii of PbF_2, which allowed containment of 98.9% of the transverse electromagnetic showers associated with the events of interest within a compact volume. Additionally, the SYMB successfully operated at the extremely high rates in the small angle region by combining very fast response PMTs (20 ns) with the fact that particles in PbF_2 produce only Čerenkov radiation, which eliminates the delay associated with a scintillation signal. Millipore paper wrapping around each crystal increased the surface reflectivity to reduce light loss and each detector resided inside a μ-metal to shield the device from the magnetic fields of the OLYMPUS toroid and the DORIS beamline.

Lead collimators, located between each detector array and the target, shielded the crystals from beam bremsstrahlung, non-symmetric Møller/Bhabha events, and other backgrounds. Each collimator consisted of a 100 mm thick lead block with a precision- machined circular hole with diameter 20.5 mm. Since these apertures determined the solid angle acceptance of each detector, the location and orientation of the collimator holes was carefully surveyed before and after each running period.

5.2.1. Readout Electronics

The SYMB readout electronics was based on a designed used for the A4 Experiment at MAMI in Mainz (33). The system provided the ability to conduct fast analog summation of the nine PMT signals from each crystal and to quickly digitize and histogram the summed signal. The detector operated at and digitally histogramed events up to a rate of 50 MHz (limited by the 20 ns signal time of the PMTs). Typical single event rates in the detectors during DORIS operation were 10 MHz, well within the operational capability of the device.

Fig. 27 shows a schematic of the readout system. First, the system summed the 9 analog signals from the crystal array and split this signal into three channels for the coincidence, master, and slave modes. Simultaneous with the summing (to accommodate the high event rate), the signals from the nine crystals were compared to determine if the center of the EM shower occurred in the center crystal to reject noise events. When this condition was satisfied in conjunction with the summed signal exceeding the threshold of a constant fraction discriminator the system generated a trigger signal for the digital histogram system. Due to the high event rate, no single events were read-out.

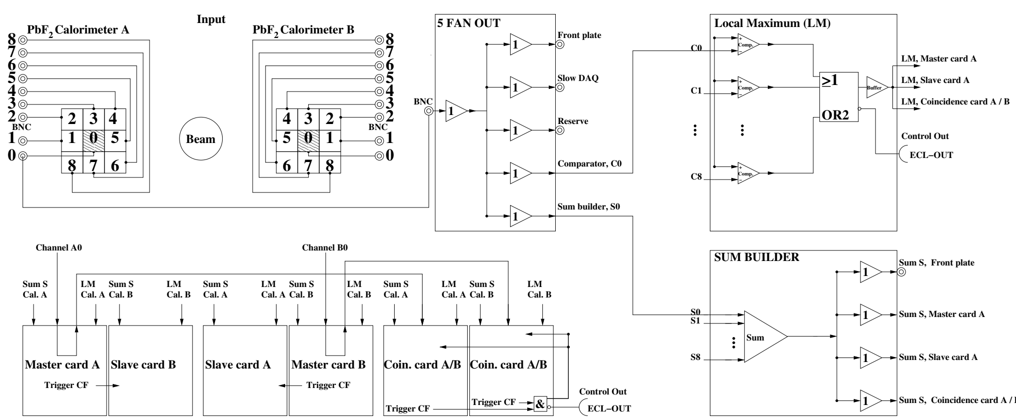

Fig. 27: A schematic of the signal flow through the SYMB data acquisition electronics.

5.2.2. Event Selection

Event selection for the SYMB detector utilized the fact that symmetric Møller, Bhabha, and annihilation events exhibited equal energy deposition in both calorimeters, while many background processes deposited energy asymmetrically. The detector generated three histograms from the recorded events. The coincidence mode required the signal from both sides to exceed the discriminator threshold, while the other two modes independently recorded single arm events over threshold. Fig. 28 shows an example of the coincidence event histograming.

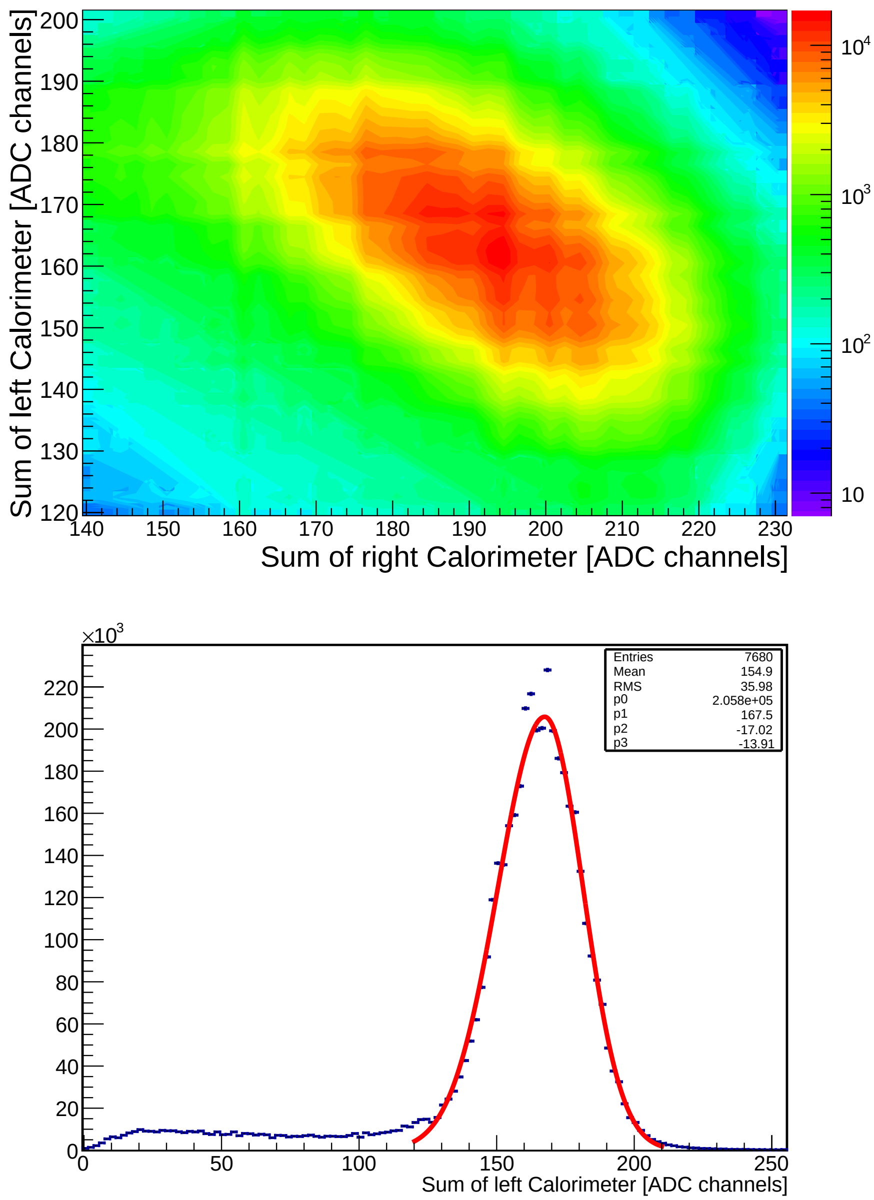

Fig. 28: Top: A 2D histogram of the sum of the deposited energy in the left and right SYMB calorimeters in coincidence mode. Bottom: A projection of the sum of the deposited energy in the left calorimeter, corrected for the differential non-linearity of the ADC.

6. Trigger

The OLYMPUS Experiment required the development of a new trigger system that incorporated information from the reused detector components from BLAST, the new luminosity detectors, as well as information from the DORIS accelerator. This was implemented using a VME field programmable gate array (FPGA), which allowed the combination of up to 16 input signals from various systems to produce 16 parallel trigger conditions, which could be prescaled to control the rate at which different conditions were recorded.

The ToF scintillator bars and the SiPMs in the 12° luminosity monitors provided the fast trigger signals for the experiment, while the DORIS accelerator provided timing information. The primary trigger signal consisted of requiring coincidence between the top and bottom PMTs of a ToF bar in both the left and right sectors of the detector. The ToFs were grouped such that the trigger signal was produced only when the relative position of the left and right bars corresponded to the expected kinematics of an elastic $e^{\pm}p$ event. The main 12° luminosity trigger consisted of a coincidence between the two SiPMs in one sector and a ToF in the opposite sector. The DORIS bunch clock was used to provide the reference time signal for the ToF and drift chamber TDCs.

In addition to the primary triggers, several signals corresponding to less strict ToF coincidences and signals from the lead glass calorimeters behind the 12° detectors were included at higher prescale factors. Events from these triggers provided means of monitoring the efficiencies and calibration of various detector components over the course of data-taking.

During the February data run, inspection of the collected data indicated that the number of elastic $e^{\pm}p$ events in the recorded data was an unsatisfactorily small fraction of the number of triggers. To improve this for the Fall run, a second-level trigger was implemented to incorporate data from the drift chambers. The TDC signals from the drift chamber sense wires in the middle and outer chambers in each side were grouped to produce a second-level trigger signal only when at least one wire in each of the middle and outer chambers on each side was hit. This signal was combined with the primary ToF trigger to form the main trigger signal for the Fall run. This scheme succeeded in reducing the false trigger rate by a factor of approximately 10, which was critical to controlling the trigger rate during high luminosity "top-up" running (see Sec. 9).

7. Data Acquisition System

The OLYMPUS data acquisition system (DAQ) utilized the framework originally developed for the Crystal Barrel Experiment at ELSA accelerator in Bonn, Germany. The implementation and hardware for the DAQ was provided by the Bonn group. The system was "synchronous" in that each detector was read-out simultaneously upon a common event signal, which ensured the event-by-event coherence of the data collected. While this approach significantly increased the complexity of the DAQ in comparison to an asynchronous system, reading the detector components synchronously conferred a number of advantages such as the ability to immediately identify readout errors from individual channels, definitive matching of data from different systems corresponding to the same event, and an overall increase in reliability of the system. Additionally, the system provided a graphical user interface for the control of data-taking and an integrated run database that was available via a web interface.

Synchronous operation was achieved via a master-slave hardware system. A schematic of the system is shown in Fig. 29. The system consisted of a number of 6U VME-Modules, one of which served as the *master*. The *master* module was responsible for monitoring the state of each of the *client* modules, each of which handled the signals from a set of detector elements. Each module contained a VME CPU for handling of the data readout. During data taking, each of the *client* modules signaled its state to the *master* via its "Busy+Okay" lines. The *master* generated an event trigger signal and distributed it to the clients only when all clients reported that they were functioning.

The signal sequence for the generation of a synchronous event signal by the DAQ is shown in Fig. 30. The *master* first sent an event request to the *client* modules, which responded by beginning the read-out of their detectors and reporting "busy" to the *master*. Upon completion of its readout, each *client* reported "Okay" to the *master*. Once all modules reported a successful readout, the *master* generated an event trigger signal.

Each of the VME CPUs associated with a *client* module corresponded to a specific subdetector (with some subdetectors requiring multiple CPUs) and served as a "local event builder" (LEVB) for that subdetector. The CPU associated with the *master* module served as the global event builder, in that it collected data from each of the LEVBs and checked the results for completeness before committing the data to disk. Communication be-

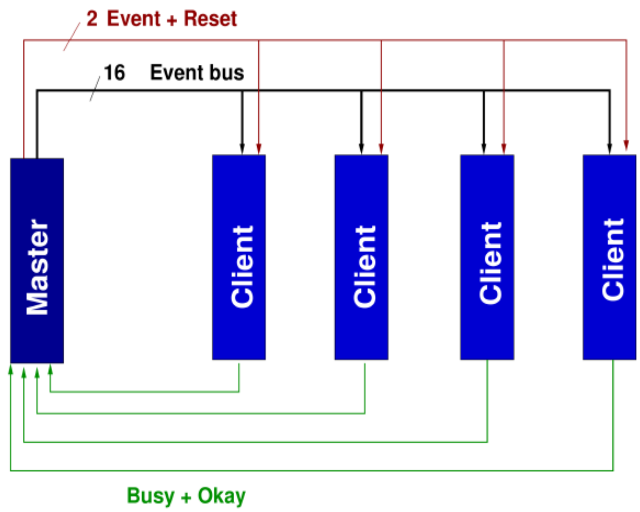

Fig. 29: Schematic of the master-slave layout of the DAQ synchronization system.

tween the global and local event builders was conducted over two dedicated 1 GBit TCP/IP networks, which allowed the separation of data transfer signals from control signals to minimize competition for bandwidth. Each of the LEVBs ran appropriate functions for interaction with the TDC, ADC, and/or scalar modules of its subdetector. The modular design of the DAQ system allowed for the construction of a synchronous readout system without excessive development time or manpower.

The global event builder featured an interchangeable output system enabling a wide variety of data formats, which provided flexibility in choosing the optimal data format for OLYMPUS.

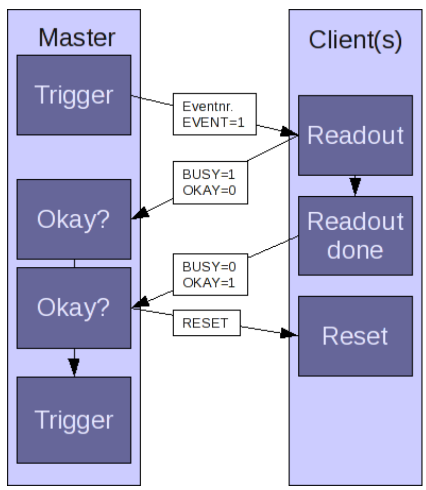

Fig. 30: Signal flow chart for the generation of an event signal in the synchronization system.

8. Slow Control

The operation of the OLYMPUS Experiment required several hundred systems to be monitored, controlled, and recorded. These included high voltage supplies, vacuum pumps and gauges, the hydrogen gas supply system, the parameters of the DORIS beam, and other elements with operational time scales on the order of second. To satisfy these requirements, a new dedicated slow control system was developed for OLYMPUS.

The slow control system utilized the Experimental Physics and Industrial Control System (EPICS)[15] as its backend solution. The system ran on three Linux machines: two VME computers with interface cards connecting to the control equipment and one server which communicated data to a PostgreSQL database and interfaced with the DORIS control system. The database recorded the status and history of all parameters associated with the slow control. The slow control also passed this data to the DAQ for integration with the detector data to produce the run data files.

The slow control system included a user-friendly, web-accessible graphical user interface, implemented using Flask as middleware. While typical slow control systems require the deployment of custom, operating system dependent software on their control computers, the design of the OLYMPUS system allowed both view-only and control access from any computer with an Internet connection. The user interface provided simple on-screen controls for the various elements connected to the system, displayed real-time plots and indicators of system statuses and data, and produced visual and audible alarms when parameters failed to satisfy proper run conditions.

[15] http://www.aps.anl.gov/epics/index.php

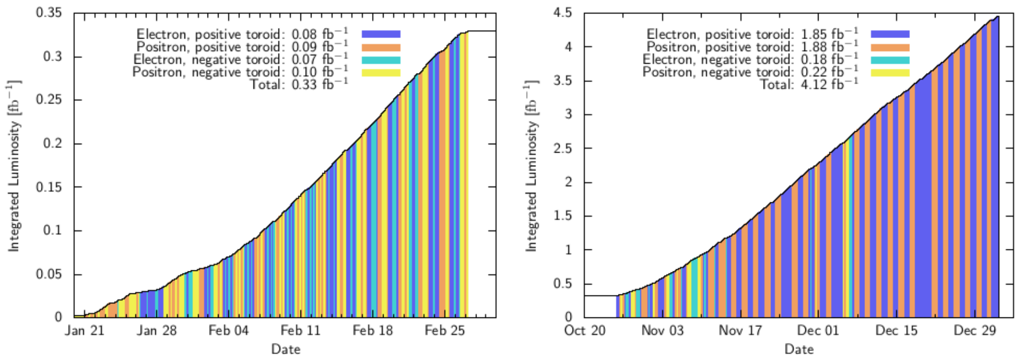

Fig. 31: The approximate integrated luminosity delivered to the OLYMPUS Experiment during the February (left) and fall (right) runs, as measured by the slow control (accurate to $\sim$10%).

9. Operation

During normal data-taking runs, a two-person shift crew operated the OLYMPUS detector and monitored the quality of the data using a number of plots generated in near real-time. Typically, production runs were taken 24 hours a day during the February and fall runs, alternating daily between positron and electrons beams. The integrated luminosity delivered to the experiment during the two runs is shown in Fig. 31. In total, a data set of approximately 4.5 fb^{-1} was collected over the course of both runs. As discussed in Sec. 1, density of gas in the target cell during the February run was significantly lower than the design value due to a leak in the interface between the H_2 gas feed system and the target cell. Due to this, less than 10% of the ultimate data set was collected during the February run. As is described in the following section, it was possible to run at higher average beam current during the fall run, which allowed the experiment to reach its initial integrated luminosity goals. At these higher currents, however, it was only possible to operate the experiment using a single toroid polarity (positive) due to the fact that low energy electrons were bent into the detectors in the negative polarity, resulting in an inoperable background level. Uptime during the data-taking runs was extremely high (approximately 95%), with most of the downtime accounted for by the time required (on the order of an hour) to switch the beam species daily.

9.1. Data Collection

As previously noted in Sec. 2, the experiment employed two modes of operation, differentiated by the manner in which the DORIS beam was operated. During the February run, the experiment was operated in "manual" mode in which the beam was initially filled to ∼65 mA and then data was taken as the beam decayed to ∼40 mA. At this point, the shift crew used the slow control interface (Sec. 8) to lower the high voltage of the various detectors to preset safe values. Since beam refills during the earlier running period were not as clean as during the fall 2012 run (more instability and losses), the lowering of the voltages prevented high voltage trips and possible damage to the detectors during the refill. After lowering the voltages, the OLYMPUS shift crew informed the DORIS accelerator crew that the detector was ready for beam refill. Once the beam was restored to the normal starting current, the voltages were brought back to operational values and data-taking was restarted.

Between the February and fall runs, significant improvements were made to the DORIS beam injection process that allowed the OLYMPUS Experiment to be run in "top-up mode." In this mode, the beam was initially filled to ∼65 mA as in the manual mode, but was only allowed to decay to ∼58 mA before triggering an automatic refill. Due to the improved injection, it was not necessary to lower the high voltage of the OLYMPUS detectors during these injections. The DAQ was configured to briefly inhibit data-taking during injection pulses (see Sec. 2). This mode of running significantly increased the average instantaneous luminosity delivered to the experiment and freed the OLYMPUS shift crew to more carefully monitor the quality of the beam and incoming data.

Due to the importance of collecting data with both positrons and electrons, the beam species was switched each morning (with occasional exceptions for maintenance, balancing the amount of data collected with each species, etc.). This ensured that there were no systematic differences between e^+ and e^- runs introduced by environmental factors such as day/night cycles, reduced traffic on the DESY campus on weekends, etc. Similarly, during the February run, in which both toroid polarities were used, data-taking was segmented into four six-hour blocks each day. The pattern of toroid polarities in the four blocks each days was selected by coin toss to ensure equal running time for each polarity while avoiding systematic effects due to the time of day and week.

In addition to production runs, empty target runs (with the H_2 gas flow shut-off and the target chamber pumped down to ring vacuum levels), zero magnetic field runs, and other test runs were taken on an approximately daily basis for the purposes of monitoring backgrounds, providing data for detector calibrations, and testing proposed changes to operations. When the DORIS beam was unavailable due to problems or maintenance, the detector was left active to collect cosmic ray data. Also, cosmic ray data were collected for approximately one month following the end of OLYMPUS production runs in January 2013. This large cosmic data set is being used for various studies of detector efficiencies and for calibration.

9.2. Data Quality Monitoring

During data-taking, the quality of the incoming data was monitored in several stages. Real-time, online monitoring of essential parameters was implemented using the ExPlORA framework originally developed by the Crystal Barrel collaboration (34). The ExPlORA program processed the raw data ZEBRA files during data collection to produce a variety of histograms and plots of quantities versus time, such as the number of drift chamber wires hit per event, ADC and TDC distributions, DAQ deadtime, and various detector rates. The OLYMPUS shift crew had access to reference plots corresponding to those shown in ExPlORA that showed data of known good quality and data representing known possible issues. This provided the shift crew with the ability to quickly identify problems with detectors as well as problems caused by poor beam quality and take action to resolve them rather than taking low-quality data.

For the fall run, a second level of data quality monitoring by the shift crew was implemented that allowed inspection of the data in a more processed format approximately 30 minutes after the conclusion of a single data run. This program automatically ran basic analysis programs on complete datasets as they became available and presented the data to the shift crew. In a similar fashion as the real-time monitoring, this program presented histograms and plots of the recent data to be compared with data of known quality, but included higher-level information such as the properties of events with good particle track candidates and basic measures of detector efficiencies.

Additionally, the long-term performance of the detector was monitored using the slow control database discussed in Sec. 8. This provided the ability to monitor the behavior of many detector parameters over the course of the entire data-taking period to identify slow drifts and sudden changes that could affect the analysis.

10. Summary

In 2012 the OLYMPUS experiment successfully collected approximately 4.5 fb^{-1} of data for electron and positron elastic scattering from hydrogen at the DORIS storage ring at DESY. The experiment used a large acceptance, left/right symmetric detector system consisting a toroidal magnetic spectrometer with drift chambers for tracking, time-of-flight scintillators for triggering and relative timing, and a redundant set of luminosity monitors. A flexible trigger and data acquisition system was used to collect the data. The left/right symmetric design of the detector and the daily alternation of beam species minimized the systematic uncertainties of the measurement. The initial plan to additionally change the toroidal magnet polarity regularly was not possible due to high background rates in the negative polarity configuration. Consequently the majority (78%) of the data were collected with positive magnet polarity.

This paper has provided a technical description of the accelerator, internal target, detector, electronics, and operation of the OLYMPUS experiment. Future papers will detail the performance of the detector, analysis, and physics results obtained.

11. Acknowledgments

The successful design, construction, and operation of the OLYMPUS experiment would not have been possible without the research and technical support staffs of all of the institutions involved. In particular, we would like to acknowledge the DORIS accelerator group for providing the high quality electron and positron beams delivered to the experiment. We also gratefully acknowledge the DESY MEA and MKK groups for providing the necessary infrastructure and support during the assembly, commissioning, operation, and disassembly of the experiment. The research and engineering group from MIT-Bates was invaluable in all phases of the experiment, from disassembling BLAST and shipping components to DESY and overcoming numerous unanticipated problems during the installation of the experiment, particularly with the target and vacuum systems.

We would like to thank E. Steffens for numerous suggestions and helpful discussions during the initial development of the experiment.

Finally, we gratefully acknowledge the DESY directorate, particularly Prof. Heuer and Prof. Mnich, and the DESY Physics Review Committee for their support, advice, and encouragement from the start of the proposal.

This work was supported by numerous funding agencies which we gratefully acknowledge: the Ministry of Education and Science of Armenia, the United Kingdom Science and Technology Facilities Council and the Scottish Universities Physics Alliance, the United States of America Department of Energy, and the Ministry of Education and Science of the Russian Federation.

References

[1] A. J. R. Puckett, others, Recoil Polarization Measurements of the Proton Electromagnetic Form Factor Ratio to $Q^2 = 8.5$ GeV^2, Phys. Rev. Lett. 104 (2010) 242301.

[2] M. Paolone, S. P. Malace, S. Strauch, I. Albayrak, J. Arrington, others, Polarization Transfer in the ^{4}He$(\vec{e}, e'\vec{p})^3$H Reaction at Q^2= 0.8 and 1.3 (GeV/c)^2, Phys. Rev. Lett. 105 (2010) 072001.

[3] B. Hu, others, Polarization transfer in the ^{2}H$(\vec{e}, e'\vec{p})n$ reaction up to Q^2 = 1.61 (GeV/c)^2, Phys. Rev. C73 (2006) 064004.

[4] M. K. Jones, others, G_{E_p}/G_{M_p} Ratio by Polarization Transfer in $\vec{e}p \rightarrow e\vec{p}$, Phys. Rev. Lett. 84 (2000) 1398–1402.

[5] G. MacLachlan, others, The ratio of proton electromagnetic form factors via recoil polarimetry at $Q^2 = 1.13$ (GeV/c)^2, Nucl. Phys. A764 (2006) 261–273.

[6] V. Punjabi, others, Proton elastic form factor ratios to $Q^2 = 3.5$ GeV^2 by polarization transfer, Phys. Rev. C71 (2005) 055202.

[7] S. Strauch, others, Polarization Transfer in the ^{4}He$(\vec{e}, e'\vec{p})^3$H Reaction up to $Q^2 = 2.6$ (GeV/c)^2, Phys. Rev. Lett. 91 (2003) 052301.

[8] O. Gayou, others, Measurement of G_{E_p}/G_{M_p} in $\vec{e}p \rightarrow e\vec{p}$ to $Q^2 = 5.6$ GeV^2, Phys. Rev. Lett. 88 (2002) 092301.

[9] I. A. Qattan, others, Precision Rosenbluth measurement of the proton elastic form factors, Phys. Rev. Lett. 94 (2005) 142301.

[10] M. E. Christy, others, Measurements of electron-proton elastic cross sections for $0.4 < Q^2 < 5.5$ (GeV/c)^2, Phys. Rev. C70 (2004) 015206.

[11] L. Andivahis, others, Measurements of the electric and magnetic form factors of the proton from Q^2= 1.75 to 8.83 (GeV/c)^2, Phys. Rev. D50 (1994) 5491–5517.

[12] R. C. Walker, B. W. Filippone, J. Jourdan, R. Milner, R. McKeown, D. Potterveld, L. Andivahis, R. Arnold, D. Benton, P. Bosted,

G. deChambrier, A. Lung, S. E. Rock, Z. M. Szalata, A. Para, F. Dietrich, K. Van Bibber, J. Button-Shafer, B. Debebe, R. S. Hicks, S. Dasu, P. de Barbaro, A. Bodek, H. Harada, M. W. Krasny, K. Lang, E. M. Riordan, Measurements of the proton elastic form factors for $1 \leq Q^2 \leq 3$ (GeV/c)^2 at SLAC, Phys. Rev. D49 (11) (1994) 5671–5689.

[13] P. A. Guichon, M. Vanderhaeghen, How to reconcile the Rosenbluth and the polarization transfer method in the measurement of the proton form-factors, Phys.Rev.Lett. 91 (2003) 142303. arXiv:hep-ph/0306007, doi:10.1103/PhysRevLett.91.142303.

[14] P. Blunden, W. Melnitchouk, J. Tjon, Two photon exchange and elastic electron proton scattering, Phys.Rev.Lett. 91 (2003) 142304. arXiv:nucl-th/0306076, doi:10.1103/PhysRevLett.91.142304.

[15] Y. C. Chen, A. Afanasev, S. J. Brodsky, C. E. Carlson, M. Vanderhaeghen, Partonic calculation of the two-photon exchange contribution to elastic electron-proton scattering at large momentum transfer, Phys. Rev. Lett. 93 (12) (2004) 122301. doi:10.1103/PhysRevLett.93.122301.

[16] A. V. Afanasev, S. J. Brodsky, C. E. Carlson, Y.-C. Chen, M. Vanderhaeghen, Two-photon exchange contribution to elastic electron-nucleon scattering at large momentum transfer, Phys. Rev. D 72 (1) (2005) 013008. doi:10.1103/PhysRevD.72.013008.

[17] P. G. Blunden, W. Melnitchouk, J. A. Tjon, Two-photon exchange in elastic electron-nucleon scattering, Phys. Rev. C 72 (3) (2005) 034612. doi:10.1103/PhysRevC.72.034612.

[18] S. Kondratyuk, P. G. Blunden, W. Melnitchouk, J. A. Tjon, Δ resonance contribution to two-photon exchange in electron-proton scattering, Phys. Rev. Lett. 95 (17) (2005) 172503. doi:10.1103/PhysRevLett.95.172503.

[19] E. Tomasi-Gustafsson, G. Gakh, Search for evidence of two photon contribution in elastic electron proton data, Phys.Rev. C72 (2005) 015209. arXiv:hep-ph/0412137, doi:10.1103/PhysRevC.72.015209.

[20] Y. M. Bystritskiy, E. A. Kuraev, E. Tomasi-Gustafsson, Structure function method applied to polarized and unpolarized electron-proton scattering: A solution of the $G_E(p)/G_M(p)$ discrepancy, Phys. Rev. C 75

(2007) 015207. doi:10.1103/PhysRevC.75.015207.
URL `http://link.aps.org/doi/10.1103/PhysRevC.75.015207`

[21] Y.-C. Chen, C.-W. Kao, S.-N. Yang, Is there model-independent evidence of the two-photon-exchange effect in the electron-proton elastic scattering cross-section?, Phys.Lett. B652 (2007) 269–274. arXiv:nucl-th/0703017, doi:10.1016/j.physletb.2007.07.044.

[22] J. Guttmann, N. Kivel, M. Meziane, M. Vanderhaeghen, Determination of two-photon exchange amplitudes from elastic electron-proton scattering data, The European Physical Journal A - Hadrons and Nuclei 47 (2011) 1–5, 10.1140/epja/i2011-11077-4.
URL `http://dx.doi.org/10.1140/epja/i2011-11077-4`

[23] M. Gorchtein, Dispersive contributions to e^+p/e^-p cross section ratio in forward regime, Physics Letters B 644 (5-6) (2007) 322–330. doi:DOI: 10.1016/j.physletb.2006.11.065.
URL `http://www.sciencedirect.com/science/article/pii/S0370269306015231`

[24] D. Borisyuk, A. Kobushkin, Box diagram in the elastic electron-proton scattering, Phys.Rev. C74 (2006) 065203. arXiv:nucl-th/0606030, doi:10.1103/PhysRevC.74.065203.

[25] H. Albrecht, others, Physics with ARGUS, Phys. Rept. 276 (1996) 223–405.

[26] D. Hasell, T. Akdogan, R. Alarcon, W. Bertozzi, E. Booth, others, The BLAST experiment, Nucl. Instrum. Meth. A603 (2009) 247–262.

[27] K. A. Dow, T. Botto, A. Goodhue, D. K. Hasell, D. Loughnan, others, Magnetic field measurements of the BLAST spectrometer, Nucl. Instrum. Meth. A599 (2009) 146–151.

[28] F. Simon, J. Kelsey, K. M, R. Majka, M. Plesko, T. Sakuma, N. Smirnov, H. Spinka, B. Surrow, S. Underwood, Beam performance of tracking detectors with industrially produced gem foils, Nucl. Instrum. Meth. A598 (2009) 432–438.

[29] M. J. French, others, Design and results from the APV25, a deep sub-micron CMOS front-end chip for the CMS tracker, Nucl. Instrum. Meth. A466 (2001) 359–365.

[30] N. Bondar, V. Golovtsov, A. Golyash, E. Lobachev, L. Uvarov, S. Uvarov, V. Yatsura, Third Generation Coordinate ReadOut System CROS-3, PNPI High Energy Physics Division Main Scientific Activities 2002-2006 (2007) 334.

[31] A. Andreev, S. Belostotsky, G. Gavrilov, O. Grebenyuk, E. Ivanov, others, Multiwire proportional chambers in the HERMES experiment, Nucl. Instrum. Meth. A465 (2001) 482–497.

[32] R. Veenhof, GARFIELD, recent developments, Nucl. Instrum. Meth. A419 (1998) 726–730.

[33] R. Kothe, Design and operation of fast calorimeter electronics for an experiment for the measurement of the parity violation in elastic electron scattering.

[34] D. M. Piontek, The new online monitor for the Crystal Barrel Experiment at ELSA, 24th Students' Workshop on Electromagnetic Interactions Bosen (Saar), 2006.